A Generalized Equatorial Model for the Accelerating Solar Wind

S. Tasnim[1] (ID), Iver H. Cairns[1] (ID), and M. S. Wheatland[1] (ID)

[1] School of Physics, The University of Sydney, Sydney, New South Wales, Australia

Abstract A new theoretical model for the solar wind is developed that includes the wind's acceleration, conservation of angular momentum, deviations from corotation, and nonradial velocity and magnetic field components from an inner boundary (corresponding to the onset of the solar wind) to beyond 1 AU. The model uses a solution of the time-steady isothermal equation of motion to describe the acceleration and analytically predicts the Alfvénic critical radius. We fit the model to near-Earth observations of the Wind spacecraft during the solar rotation period of 1–27 August 2010. The resulting data-driven model demonstrates the existence of noncorotating, nonradial flows and fields from the inner boundary ($r = r_s$) outward and predicts the magnetic field $\mathbf{B} = (B_r, B_\phi)$, velocity $\mathbf{v} = (v_r, v_\phi)$, and density $n(r, \phi, t)$, which vary with heliocentric distance r, heliolatitude ϕ, and time t in a Sun-centered standard inertial plane. The description applies formally only in the equatorial plane. In a frame corotating with the Sun, the transformed velocity $\mathbf{v}'$ and a field $\mathbf{B}'$ are not parallel, resulting in an electric field with a component E'_z along the z axis. The resulting $\mathbf{E}' \times \mathbf{B}' = \mathbf{E}' \times \mathbf{B}$ drift lies in the equatorial plane, while the ∇B and curvature drifts are out of the plane. Together these may lead to enhanced scattering/heating of sufficiently energetic particles. The model predicts that deviations δv_ϕ from corotation at the inner boundary are common, with $\delta v_\phi(r_s, \phi_s, t_s)$ comparable to the transverse velocities due to granulation and supergranulation motions. Abrupt changes in $\delta v_\phi(r_s, \phi_s, t_s)$ are interpreted in terms of converging and diverging flows at the cell boundaries and centers, respectively. Large-scale variations in the predicted angular momentum demonstrate that the solar wind can drive vorticity and turbulence from near the Sun to 1 AU and beyond.

1. Introduction

The outflow of heated ions and electrons from the expanding outer atmosphere of the Sun is referred to as the solar wind. The solar wind originates from an effective "inner boundary," with properties that vary with heliolatitude and heliolongitude but are often assumed to be constant over a solar rotation period. This causes the wind to rotate as a spatially varying but time-constant pattern across an observer as the Sun rotates. The solar wind plasma is highly conducting and the magnetic field is frozen-in to the plasma. Rotation of the Sun then leads naturally to spiral-like magnetic field lines (Parker, 1958). Recent work shows, though, that the usual Parker spiral is often not a good approximation (Borovsky, 2010; Forsyth et al., 1996; Li, Cairns, Gosling, Malaspina, et al., 2016; Li, Cairns, Gosling, Steward, et al., 2016; Schulte in den Bäumen et al., 2011, 2012).

Over the past few decades, a great effort has been made to better understand the physical processes responsible for solar wind properties, along with their qualitative and quantitative interpretations. Important solar wind characteristics that have gained the most interest include: (1) the acceleration and heating of the solar wind close to the Sun (from 2 to 10 solar radii) (Coles, 1995; Cranmer, 2002a, 2002b; Hakamada & Kojima, 1994; Kohl et al., 1997; Tu et al., 2005), (2) deviations from the Parker spiral orientation at different spatial and temporal scales in most observations (Borovsky, 2010; Forsyth et al., 1996; Schulte in den Bäumen et al., 2011, 2012; Tasnim & Cairns, 2016), even though the Parker spiral agrees well with observations when averaged over many rotations (Forsyth et al., 1996; Smith, 1979; Thomas & Smith, 1980), (3) the existence of nonradial intrinsic magnetic fields (De Pontieu et al., 2011; Petrie & Patrikeeva, 2010) and velocities (Fisk, 1996; Richardson et al., 1996; Tasnim & Cairns, 2016; Weber & Davis, 1967) at the inner boundary, where the word "intrinsic" means that these velocities and fields exist in the plasma at the inner boundary due to unspecified physical processes at smaller radial distances, (4) magnetohydrodynamic (MHD) turbulence in the corona and solar wind (Bruno & Carbone, 2005; Goldstein & Roberts, 1995; Usmanov et al., 2000; Usmanov & Goldstein, 2003; Zank & Matthaeus, 1991, 1992, 1993), and (5) the location of the Alfvénic critical surface (r_A)

(DeForest et al., 2014; Tasnim & Cairns, 2016). Note that the Alfvénic critical surface r_A is defined as a locus of Alfvénic critical radius where the flow speed is equal to the Alfvén speed V_A.

Models for the solar wind generally assume that magnetic field lines are parallel to flow stream lines in the frame corotating with the Sun (Parker, 1958; Weber & Davis, 1967). However, this assumption requires the electric field in the rotating reference frame to be zero ($\mathbf{E}' = 0$ in the equatorial plane). Later, the models for the solar wind by Keppens and Goedbloed (1999) and Hu et al. (2003) improved the Parker (1958) and Weber and Davis (1967) models and provided a more detailed picture of the solar wind by including azimuthal and poloidal components for the velocity and magnetic field. In addition, the Hu et al. (2003) model focused on including colatitudinal variations while Keppens and Goedbloed (1999) introduced spatial variations described by polytropic indices. However, both of the Keppens and Goedbloed (1999) and Hu et al. (2003) models require a zero polar electric field in the rotating frame ($E'_\theta = 0$ which implies $E'_z = 0$ in the equatorial plane) and parallel flow streamlines and magnetic field lines in the meridional plane. Further, the Hu et al. (2003) model assumed the initial condition of a nonzero radial electric field component in the corotating frame ($E'_r = 0$).

Research on three-dimensional numerical models and global MHD simulations increasingly provide more realistic coronal and solar wind descriptions. These simulations enable us to address space weather conditions in a sophisticated way (Cohen, 2015; Cohen et al., 2007, 2008; Downs et al., 2010; Groth et al., 2000; Linker et al., 1999; Mikić et al., 1999; Oran et al., 2013; Roussev et al., 2003, 2004; Suess et al., 1999; Usmanov, 1993; Usmanov et al., 2000; van der Holst et al., 2010; Wu et al., 1999). Some of these simulations are fully three dimensional and successfully describe various solar wind, coronal, and space weather phenomena by including increasingly complex coronal and solar wind physics. Examples include an empirical heating source term (Groth et al., 2000; Mikić et al., 1999; Usmanov, 1993; Suess et al., 1999), Alfvén wave turbulence in the Wentzel-Kramers-Brillouin approximation (Usmanov et al., 2000; Usmanov & Goldstein, 2003), solar magnetogram data (Linker et al., 1999; Roussev et al., 2003, 2004) to model the solar wind's magnetic structures, and energy gains due to changes in polytropic index (Roussev et al., 2003) to describe the acceleration and heating of the solar wind. However, many of these numerical simulation results are not yet supported by analytic models. Additionally, development of analytic predictions will help to explain the underlying physics of numerical results and will also provide more accurate and physical ways to initialize the codes.

This paper develops a new equatorial, data-driven analytic model that generalizes the previous works of Parker (1958), Weber and Davis (1967), Jokipii and Kóta (1998), Schulte in den Bäumen et al. (2011, 2012), and Tasnim and Cairns (2016) by including the radial acceleration of the wind, conservation of angular momentum, intrinsic nonzero azimuthal velocities and magnetic fields from the inner boundary outward, and a deviation from corotation at the inner boundary. The deviation $\delta v_\phi(r_s, \phi_s)$ can be due to motions associated with granulation and supergranulation cells (Schulte in den Bäumen et al., 2011, 2012; Jokipii & Kóta, 1998; Jokipii & Parker, 1968), where r_s is the radius of the inner boundary and ϕ_s is the corresponding phase angle. We find that the predicted deviations are sometimes strong enough to cancel the corotation effects or to change the flow patterns. The model also predicts the Alfvénic critical radius $r_A(\phi_a)$, where $r_A(\phi_a)$ is defined as the locus of the Alfvénic critical radii as a function of phase angle ϕ_a (where ϕ_a presents the phase angle corresponding to the Alfvénic critical radius). The model fits show that the velocity $\mathbf{v}'$ is not always parallel to the magnetic field $\mathbf{B}'$ in the corotating frame, leading to nonzero predicted electric fields E'_z in the z direction in the corotating frame at all r, and so effects on energetic particle motion are expected.

The new data-driven analytic model provides a more complete description of the solar wind and should enable a better understanding of solar wind properties via theory-data and simulation-data comparisons. This model is the first analytic theoretical attempt to simultaneously treat the acceleration of the solar wind, permit a deviation from corotation at the inner boundary, include intrinsic nonradial velocity and magnetic field from the inner boundary to 1 AU and beyond, and enforce conservation of angular momentum. It generalizes the existing theoretical solar wind models (Jokipii & Kóta, 1998; Parker, 1958; Schulte in den Bäumen et al., 2011, 2012; Tasnim & Cairns, 2016; Weber & Davis, 1967) by relaxing the assumptions of constant radial speed, strong corotation, zero electric field in the corotating frame, and so on. Therefore, this model improves the preceding models, specifically, the new model relaxes the assumptions of purely radial magnetic field (Hu et al., 2003; Jokipii & Kóta, 1998; Keppens & Goedbloed, 1999; Parker, 1958; Weber & Davis, 1967) and velocity (Jokipii & Kóta, 1998; Parker, 1958; Schulte in den Bäumen et al., 2011, 2012) at the inner boundary, constant radial speed (Jokipii & Kóta, 1998; Schulte in den Bäumen et al., 2011, 2012; Tasnim & Cairns, 2016;

Weber & Davis, 1967), $\mathbf{E}' = 0$ (Parker, 1958; Weber & Davis, 1967), neglect of conservation of angular momentum (Parker, 1958; Schulte in den Bäumen et al., 2011, 2012), and an azimuthal flow, which is only due to the corotation of the solar wind (Tasnim & Cairns, 2016). The model's predictions are relatively insensitive to different choices of r_s, from the photosphere $R_\odot$ to any reasonable value of r. Therefore, the extracted accelerating radial wind speed, intrinsic nonradial velocities and magnetic fields should provide more realistic initial boundary conditions at $R_\odot$ for future simulations, cf. van der Holst et al. (2010), Oran et al. (2013), and Feng et al. (2015). Moreover, the model will test the simulation results and explore the physical mechanisms underlying them. Finally, the upcoming Solar Probe Plus (SPP) and Solar Orbiter space missions will provide an opportunity to test the accelerating wind model's predictions with direct observations.

The paper is structured as follows. Section 2 discusses the basic equations and assumptions of the accelerating solar wind model. Section 3 develops the new theoretical model by applying Parker's accelerating wind solution in a MHD description that conserves angular momentum and satisfies the frozen-in field condition. Section 4 solves the equations for the new solar wind model to find the analytic and numerical solutions for the plasma and field quantities from r_s to all r. Section 5 fits the model to data at 1 AU over a solar rotation in order to investigate the predictions for $r_A(\phi_a, t_a)$, the electric field in the corotating frame (E'_z), the intrinsic $v_\phi(r_s, \phi_s, t_s)$ and $B_\phi(r_s, \phi_s, t_s)$, and the variations of radial and longitudinal velocity and magnetic field. Section 5.1 shows that the predictions for r_A agree well with the observations of DeForest et al. (2014) and are semiquantitatively consistent with Tasnim & Cairns's (2016) model. Section 5.2 shows that deviations $\delta v_\phi(r_s, \phi_s)$ from corotation are generally present and have significant implications. It also shows that the predictions for $B_\phi(r_s, \phi_s, t_s)$ are different from but semiquantitatively consistent with the predictions from previous solar wind models (Schulte in den Bäumen et al., 2011, 2012; Tasnim & Cairns, 2016), and it demonstrates that sometimes the predicted values of $\delta v_\phi(r_s, \phi_s, t_s)$ cancel out the azimuthal speed due to corotation. The sudden changes in δv_ϕ are interpreted in terms of converging and diverging flows associated with granulation and supergranulation cells. Section 5.3 describes the radial profiles of $v_\phi(r, \phi, t)$ and $B_\phi(r, \phi, t)$. Section 5.4 predicts that the angular momentum per unit mass $\mathbf{L}$ varies greatly with longitude but agrees semiquantitatively with the predictions of Weber and Davis (1967) and can act as a source of turbulence. Section 5.5 demonstrates that the model predicts nonzero E'_z, in general, in contrast to the widely used assumption of $\mathbf{E}' = 0$. This means that magnetic field lines are not velocity streamlines in general. Subsection 5.6 calculates the power law index $\gamma(\phi)$ of the temperature profile for a selected solar rotation period, fitting a mean value very close to the standard empirical value, showing the differences from the constant speed solar wind model and the longitudinal (ϕ) variations in E'_z, L_z, B_ϕ, n_i, $v_r(r)$, and $T_i(r)$. Section 5.7 illustrates the global plasma and field environment. Section 6 discusses the results and concludes the paper.

2. Basic Equations and Assumptions for the Accelerating Solar Wind Model

2.1. Basic Equations in Inertial and Rotating Frames

This model combines an accelerating v_r profile for an isothermal wind with the magnetohydrodynamic (MHD) equations for conservation of mass and angular momentum, frozen-in magnetic fields, Gauss's Law for magnetism $\nabla \cdot \mathbf{B} = 0$, and Faraday's Law $\nabla \times \mathbf{E} = -\partial \mathbf{B}/\partial t$, where $\mathbf{E}$ is the electric field.

Starting from a spherical coordinate system in which r, ϕ, and θ represent radial, azimuthal (longitudinal), and polar (latitudinal) components, respectively, we restrict attention to the equatorial plane (r, ϕ) in an inertial frame. Assuming that the θ components are negligible in the (r, ϕ) plane, the fluid motion $\mathbf{v}$ and magnetic field $\mathbf{B}$ only have nonzero components v_r, v_ϕ, B_r, and B_ϕ, all of which depend on r and ϕ in general. This neglect may not be always justified; for example, the B_θ or north-south component of $\mathbf{B}$ is known to be important for space weather and is often large in coronal mass ejection (CME) events. Similarly, v_θ is comparable to v_ϕ during CME and corotating interaction region events. However, neglecting B_θ and v_θ in the equatorial or ecliptic plane is typical in analytic solar wind models (Parker, 1958; Schulte in den Bäumen et al., 2011, 2012; Tasnim & Cairns, 2016; Weber & Davis, 1967).

We now transform the above equations in a 2-D equatorial inertial frame (unprimed variables) into equivalent equations for (primed) variables in a 2-D equatorial frame rotating with the Sun. The standard relations between the inertial and rotating frame are $\phi' = \phi - \Omega t$ and $r = r'$. Note that $\Omega = 2\pi/T$ denotes the Sun's rotation frequency where T is the Sun's synodic rotation period (we assume $T = 27$ days). In addition, in the nonrelativistic regime the assumption $\mathbf{B} = \mathbf{B}'$ is justified. Below in section 2.2, we justify our assumption

that time variations in the inertial frame variables correspond to variations ϕ' of a fixed spatial pattern in the rotating frame. Quantities in the rotating inertial frames are related according to

$$v_r(r, \phi, t) = v'_r(r, \phi - \Omega t) = v'_r(r', \phi'), \tag{1}$$

$$v_\phi(r, \phi, t) = v'_\phi(r, \phi - \Omega t) + r\Omega = v'_\phi(r', \phi') + \Omega r, \tag{2}$$

$$\rho(r, \phi, t) = \rho'(r, \phi - \Omega t) = \rho'(r', \phi'), \tag{3}$$

$$B_r(r, \phi, t) = B'_r(r, \phi - \Omega t) = B'_r(r', \phi'), \tag{4}$$

$$B_\phi(r, \phi, t) = B'_\phi(r, \phi - \Omega t) = B'_\phi(r', \phi'), \tag{5}$$

$$\mathbf{B}(r, \phi, t) = B'_r(r, \phi - \Omega t)\mathbf{e}_r + B'_\phi(r, \phi - \Omega t)\mathbf{e}_\phi = \mathbf{B}'(r', \phi'), \tag{6}$$

$$\mathbf{v}(r, \phi, t) = v'_r(r, \phi - \Omega t)\mathbf{e}_r + v'_\phi(r, \phi - \Omega t)\mathbf{e}_\phi + r\Omega\mathbf{e}_\phi = \mathbf{v}(r', \phi') + \Omega r\mathbf{e}_\phi, \tag{7}$$

where ρ is the mass density and $\mathbf{v}$ is the velocity. Using the relation $\phi' = \phi - \Omega t$, derivatives of an arbitrary function f in the inertial frame are related to the derivatives in the corotating frame by

$$\frac{\partial}{\partial t}f(r, \phi, t) = -\Omega\frac{\partial}{\partial \phi'}f'(r', \phi'), \tag{8}$$

$$\frac{\partial}{\partial r}f(r, \phi, t) = \frac{\partial}{\partial r'}f'(r', \phi'), \tag{9}$$

$$\frac{\partial}{\partial \phi}f(r, \phi, t) = \frac{\partial}{\partial \phi'}f'(r', \phi'). \tag{10}$$

With the variables and transformations defined, we start with the MHD equation for mass conservation:

$$\frac{d\rho}{dt} + \boldsymbol{\nabla} \cdot (\rho\mathbf{v}) = 0. \tag{11}$$

In a spherical polar coordinate system this can be written as

$$\frac{d\rho}{dt} + \left[\frac{1}{r^2}\frac{\partial}{\partial r}(\rho r^2 v_r) + \frac{1}{r\sin\theta}\frac{\partial}{\partial\theta}(\rho v_\theta \sin\theta) + \frac{1}{r\sin\theta}\frac{\partial(\rho v_\phi)}{\partial\phi}\right] = 0. \tag{12}$$

The assumption that $v_\theta = 0$ in the solar equatorial plane ($\theta = 90°$) simplifies (12) to

$$\frac{d\rho}{dt} + \left[\frac{1}{r^2}\frac{\partial}{\partial r}(\rho r^2 v_r) + \frac{1}{r}\frac{\partial \rho v_\phi}{\partial\phi}\right] = 0. \tag{13}$$

To write the mass conservation equation in the rotating frame in the equatorial plane, we use (1)–(7) and (8)–(10), whence (13) reduces to

$$\frac{1}{r'^2}\frac{\partial}{\partial r'}(r'^2\rho'v'_r) + \frac{1}{r'}\frac{\partial(\rho'v'_\phi)}{\partial\phi'} = 0. \tag{14}$$

In spherical polar coordinates with $v_\theta = 0$ and $B_\theta = 0$, Gauss's Law of magnetism ($\boldsymbol{\nabla} \cdot \mathbf{B} = 0$) in the equatorial plane, can be written as

$$\frac{1}{r^2}\frac{\partial}{\partial r}(r^2 B_r) + \frac{1}{r}\frac{\partial B_\phi}{\partial\phi} = 0. \tag{15}$$

In a rotating frame, (15) becomes

$$\frac{1}{r'^2}\frac{\partial}{\partial r'}(r'^2 B'_r) + \frac{1}{r'}\frac{\partial B'_\phi}{\partial\phi'} = 0. \tag{16}$$

We use the generalized form of Ohm's Law to write the electric field $\mathbf{E}$. Using this expression, Faraday's Law in the inertial frame reduces to

$$\frac{\partial\mathbf{B}}{\partial t} = \boldsymbol{\nabla} \times (\mathbf{v} \times \mathbf{B}) + D_B\nabla^2\mathbf{B}. \tag{17}$$

In (17), we assume that the Hall effect, electron inertial term, and pressure gradient term have negligible effects on curl **E**. Here D_B is the magnetic diffusion coefficient, $\mathbf{E} = -\mathbf{v} \times \mathbf{B}$, $\nabla \times (\mathbf{v} \times \mathbf{B})$ is the magnetic convective term, and $D_B \nabla^2 \mathbf{B}$ is the diffusive term, respectively. This plasma is assumed to be highly conductive, so the conductive term dominates the diffusive term. This results in the magnetic field moving with the plasma, that is,

$$\frac{\partial \mathbf{B}}{\partial t} = \nabla \times (\mathbf{v} \times \mathbf{B}). \tag{18}$$

From (18), the frozen-in field condition in the inertial frame is

$$\mathbf{E} = -\mathbf{v} \times \mathbf{B}. \tag{19}$$

We can write (19) as

$$\mathbf{E} = -(\mathbf{v} \times \mathbf{B}),$$
$$= -\mathbf{v}_p \times B_\phi \mathbf{e}_\phi - v_\phi \mathbf{e}_\phi \times \mathbf{B}_p - \mathbf{v}_p \times \mathbf{B}_p, \tag{20}$$

where $\mathbf{v}_p = v_r \mathbf{e}_r + v_\theta \mathbf{e}_\theta$ (in spherical coordinates) $= v_r \mathbf{e}_r + v_z \mathbf{e}_z$ (in cylindrical coordinates) is the poloidal component of the flow velocity and $\mathbf{B}_p = B_r \mathbf{e}_r + B_\theta \mathbf{e}_\theta = B_r \mathbf{e}_r + B_z \mathbf{e}_z$ is the poloidal magnetic field. Here $\mathbf{e}_\phi$, $\mathbf{e}_r$, $\mathbf{e}_\theta$, and $\mathbf{e}_z$ denote unit vectors in the relevant directions. Again, assuming $B_\theta = 0$ and $v_\theta = 0$ in the solar equatorial plane ($\theta = 90°$), and that the solar equatorial plane is a cylindrical disk with $h \to 0$ (where h represents the height of a cylinder), the frozen-in field condition in cylindrical coordinate for the magnetized wind reduces to

$$\mathbf{E} = (-v_r B_\phi + v_\phi B_r)\mathbf{e}_z = (-v_r B_\phi + v_\phi B_r)\mathbf{e}_\theta. \tag{21}$$

Similarly, the electric field in the corotating frame is

$$\mathbf{E}' = (-v_r' B_\phi' + v_\phi' B_r')\mathbf{e}_z = (-v_r' B_\phi' + v_\phi' B_r')\mathbf{e}_\theta. \tag{22}$$

Therefore, (21) and (22) allow us to relate the electric field E_z in the inertial frame with the field E_z' in the corotating frame:

$$E_z' = E_z - \Omega r \sin\theta B_r. \tag{23}$$

Note that in the equatorial plane $\theta = 90°$, which allows us to write $E_\theta' = E_z'$. Equation (23) agrees with the standard relation,

$$\mathbf{E}' = \mathbf{E} + \mathbf{v}_{\mathrm{rel}} \times \mathbf{B}, \tag{24}$$

or

$$E_z' \mathbf{e}_z = E_z \mathbf{e}_z + \Omega r \sin\theta \mathbf{e}_\phi \times B_r \mathbf{e}_r. \tag{25}$$

Combining (18) and (21), we write

$$\frac{\partial B_r}{\partial t}\mathbf{e}_r + \frac{\partial B_\phi}{\partial t}\mathbf{e}_\phi = -\frac{1}{r}\frac{\partial}{\partial \phi}\left[-v_r B_\phi + v_\phi B_r\right]\mathbf{e}_r + \frac{1}{r}\frac{\partial}{\partial r}\left[r(v_r B_\phi + v_\phi B_r)\right]\mathbf{e}_\phi. \tag{26}$$

Then, transforming (26) into the rotating frame yields

$$-\Omega\frac{\partial B_\phi'}{\partial \phi'}\mathbf{e}_\phi = -\frac{1}{r}\frac{\partial}{\partial \phi'}\left[-v_r' B_\phi' + v_\phi' B_r'\right]\mathbf{e}_r + \frac{1}{r'}\frac{\partial}{\partial r'}\left[r'(v_r' B_\phi' + v_\phi' B_r' + \Omega r' B_r')\right]\mathbf{e}_\phi, \tag{27}$$

where the $\partial B_r / \partial t$ term becomes $-\Omega \partial B_r / \partial \phi'$ and cancels with a term from the right-hand side of (27).

The MHD equation for the conservation of angular momentum including gravity (Tasnim & Cairns, 2016) in an inertial frame is

$$\frac{\partial \mathbf{L}_\star}{\partial t} + \mathbf{r} \times \nabla\left(P + \frac{B^2}{2\mu_0}\right) + \rho\mathbf{r} \times (\mathbf{v} \cdot \nabla)\mathbf{v} = \frac{1}{\mu_0}\mathbf{r} \times (\mathbf{B} \cdot \nabla)\mathbf{B}, \tag{28}$$

where $\partial \mathbf{L}_\star / \partial t$ is the time derivative of the angular momentum $\mathbf{L}_\star = \rho(\mathbf{r} \times \mathbf{v})$, and $B^2/2\mu_0$ is the magnetic pressure in the corotating frame. We assume that the distribution of particles is sufficiently random that the pressure tensor can be approximated as a scalar pressure P. A more detailed derivation is available

in Tasnim and Cairns (2016). Note that the gravitational acceleration $\mathbf{g}$ and the acceleration due to the reaction of the centripetal force have only radial dependence and are radially symmetric, so that their contributions to the torque in (28) are zero.

Assuming radially symmetric thermal and magnetic pressures (Tasnim & Cairns, 2016), (28) becomes

$$\frac{\partial \mathbf{L}_\star}{\partial t} + \rho \mathbf{r} \times (\mathbf{v} \cdot \nabla)\mathbf{v} = \frac{1}{\mu_0} \mathbf{r} \times (\mathbf{B} \cdot \nabla)\mathbf{B}. \tag{29}$$

The θ component of (29) is

$$-\frac{\partial L_{\star\theta}}{\partial t} - \rho r \left[v_r \frac{\partial v_\phi}{\partial r} + \frac{v_\phi}{r}\frac{\partial v_\phi}{\partial \phi} + \frac{v_\phi v_r}{r} \right] = -\frac{1}{\mu_0} r \left[B_r \frac{B_\phi}{\partial r} + \frac{B_\phi}{r}\frac{\partial B_\phi}{\partial \phi} + \frac{B_\phi B_r}{r} \right]. \tag{30}$$

Transforming (30) to the rotating frame and associated variables lead to

$$-\Omega v'_\phi r' \frac{\partial \rho'}{\partial \phi'} - \Omega r'^2 \frac{\partial \rho'}{\partial \phi'} + \rho' r' v'_r + \rho' r' v'_r \frac{\partial v'_\phi}{\partial r'} + 2\rho' r' v'_r \Omega$$
$$+ \rho' v'_\phi \frac{\partial v'_\phi}{\partial \phi'} + \rho' v'_\phi v'_r = \frac{1}{\mu_0} r' \left(B'_r \frac{B'_\phi}{\partial r'} + \frac{B'_\phi}{r'}\frac{\partial B'_\phi}{\partial \phi'} + \frac{B'_\phi B'_r}{r'} \right). \tag{31}$$

The time-independent equation of motion chosen for the fluid (Parker, 1958) is

$$\frac{(v_r^2 - c_s^2)}{v_r}\frac{dv_r}{dr} = \frac{2c_s^2}{r} - \frac{GM_\odot}{r^2}, \tag{32}$$

where $v_r = v_r(r, \phi, t)$, $c_s = c_s(\phi, t)$ is the sound speed, and the final term describes gravitational effects. Note that (32) assumes magnetic terms are unimportant for acceleration of the solar wind. Assuming the plasma is approximately isothermal (Parker, 1958) for each ϕ, the transonic solution has $v_r(r, \phi, t) = c_s(\phi, t)$ at the sonic radius

$$r_{so}(\phi, t) = \frac{GM_\odot}{2c_s^2(\phi, t)}. \tag{33}$$

Integrating (32) yields the Bernoulli integral for an isothermal wind (Parker, 1958):

$$\frac{v_r^2}{c_s^2} - \ln\left(\frac{v_r^2}{c_s^2}\right) = 4\ln\left(\frac{r}{r_{so}}\right) + 4\frac{r_{so}}{r} + C_4, \tag{34}$$

where C_4 is the integration constant. This equation defines the wind velocity v_r as a function of r.

In the equatorial plane model, (34) can be written as

$$\frac{v_r^2(r, \phi, t)}{c_s^2(\phi, t)} - \ln\left(\frac{v_r^2(r, \phi, t)}{c_s^2(\phi, t)}\right) = 4\ln\left(\frac{r}{r_{so}}\right) + 4\frac{r_{so}}{r} + C_4(\phi). \tag{35}$$

In the corotating frame, (35) corresponds to

$$\frac{v_r'^2(r', \phi')}{c_s'^2(\phi')} - \ln\left(\frac{v_r'^2(r', \phi')}{c_s'^2(\phi')}\right) = 4\ln\left(\frac{r'}{r'_{so}}\right) + 4\frac{r'_{so}}{r'} + C_5(\phi'), \tag{36}$$

where $c_s'(\phi') = c_s(\phi, t)$, and $C_5(\phi')$ is a function of ϕ'.

2.2. Assumptions

Synoptic magnetograms change slowly from one solar rotation to the next (Neugebauer et al., 2002), so we assume that sources of the solar wind are constant over a solar rotation, thereby producing a spatially variable but time-stationary pattern that rotates with the Sun. In such a system there is no intrinsic time variation for an observer rotating with the Sun. However, this fixed pattern moves across a noncorotating observer, such as the Earth or the Wind spacecraft. The apparent time variations in the rotating frame seen then correspond to ϕ' variations of the time-stationary pattern, as in (8). Accordingly, the time when a particular part of the pattern reaches the observer corresponds to a particular phase angle ϕ' or longitude of the solar wind pattern. Put in other way, while the plasma quantities and magnetic fields are time-stationary in the rotating frame,
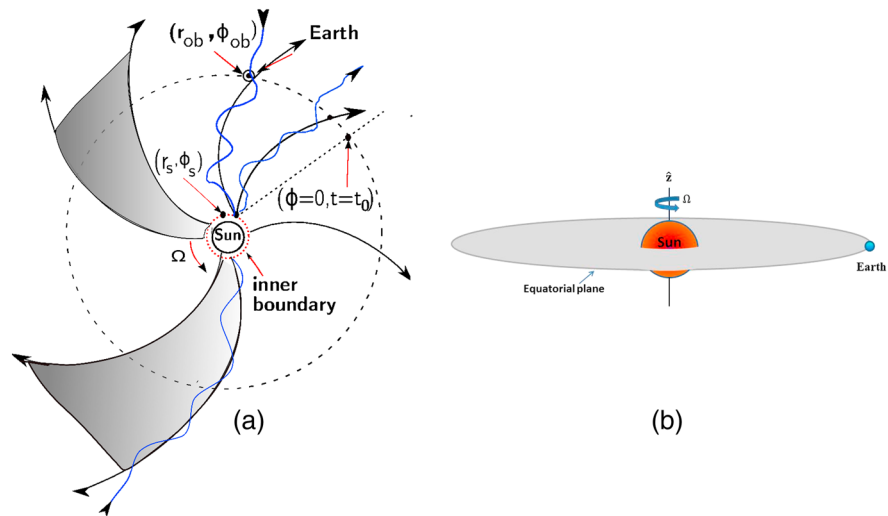
Figure 1. Illustration of the physical model for the solar wind over one solar rotation, showing magnetic field lines in the solar equatorial plane from the inner boundary (r_s, ϕ_s) to the observation locations (r_{ob}, ϕ_{ob}) and the location corresponding to the origin in time (t). Figure 1a shows the view from above the North Pole of the Sun, with the wiggly field lines emphasizing that azimuthal symmetry is not assumed, while Figure 1b shows the relative positions of the Sun, the Earth, and the solar equatorial disk (with a height $h \to 0$). Shaded portions of the figure show two stream tubes that correspond to a particular source region for the wind.

they are time-dependent quantities for an observer in an inertial frame. Specifically, the coordinates in the corotating and inertial frames are related by $r' = r$ and $\phi' = \phi - \Omega t$.

Figure 1a illustrates magnetic field lines in the equatorial plane that start at the inner boundary and end at 1 AU. The figure also illustrates the relation between the longitude ϕ and the start time $t = t_0$ when $\phi = 0$. Figure 1b shows the Sun-Earth orientation in the solar equatorial plane. The magnetic field lines in Figure 1a have azimuthal asymmetries, which are allowed by the models developed below and by Schulte in den Bäumen et al. (2011), Schulte in den Bäumen et al. (2012), Tasnim and Cairns (2016), and Li, Cairns, Gosling, Steward, et al. (2016). From the point of view of the (r, ϕ, t) and (r', ϕ') coordinate systems for the inertial and corotating frames, the variables (r, ϕ, t) are mutually independent variables, as are r' and ϕ'.

In order to relate the various ϕ and variables, the observation at time t_{ob} is assumed to be related to inner boundary (r_s) at the time t_s when the plasma left the model inner boundary r_s near the Sun, by the relation

$$t_s = t_{ob} - (1\,\text{AU} - r_s)/v_{av}. \tag{37}$$

Here v_{av} is the rotation-averaged radial speed, which is used instead of $v_r(r, \phi)$ to prevent the streamlines from crossing. The solar wind quantities at the inner boundary r_s at phase angle ϕ_s are related to the observation distance $r_{ob} = 1$ AU, longitude $\phi_{ob}(t_{ob}) = \phi_{AU} = \Omega(t_{ob} - t_0)$, and to the start time t_0 of the rotation interval $[t_0,\ t_0 + 27\ \text{days}]$ by

$$\phi_s(t_s) = \phi(1\,\text{AU}) - \frac{(1\,\text{AU} - r_s)\Omega}{v_{av}} = \Omega(t_{ob} - t_0) - \frac{(1\,\text{AU} - r_s)\Omega}{v_{av}}, \tag{38}$$

and at any other r from r_s to 1 AU by

$$\phi(r, t) = \phi_s(t_s) + \frac{(r - r_s)\Omega}{v_{av}}. \tag{39}$$

Equations (38) and (39) assume that the longitudinal meridian $\phi_s = 0$ faces the Earth at time $t = t_0$. In terms of rotating variables, the longitude at (r', ϕ') in the rotating frame obey

$$\phi'(r') = \phi'_s + \frac{(r' - r'_s)\Omega}{v'_{av}} - \Omega t, \tag{40}$$

where $\phi'_s = \phi_s(t_s) - \Omega t_s$.

This model allows us to follow approximate (velocity) streamtubes that correspond to a particular source region for the wind in which the mass, magnetic flux, and angular momentum are conserved. The electric field

in the corotating frame is also constant in the streamtube. Magnetic field lines do not always follow stream-tubes. Note that a streamtube is a region of plasma surrounded by streamlines where streamlines do not intersect with each other and the same streamlines pass through a streamtube at all points along its length. Shaded areas on Figure 1 are showing two streamtubes.

3. Accelerating Solar Wind Model

We now develop a detailed model for the accelerating solar wind using the equations and assumptions in sections 2.1 and 2.2, respectively.

We assume $\partial(\rho' v'_\phi)/\partial\phi' = 0$ in (14) in the corotating frame (Schulte in den Bäumen et al., 2011, 2012; Tasnim & Cairns, 2016), either for all ϕ' or locally, for a limited range of ϕ'. Put in other words, we assume $\rho' v'_\phi$ is constant along ϕ' within a streamtube (Figure 1). Hence, mass conservation for approximately radial flow with radial speed $v'_r(r', \phi')$ requires that the mass density $\rho' = m\, n'(r', \phi')$, where m is the mean particle mass and n' is the number density, together with the radial component of the flow $v'_r(r', \phi')$ in the corotating frame obey

$$\rho' r'^2 v'_r(r', \phi') = m\, n'(r', \phi')\, r'^2\, v'_r(r', \phi') = C_1(\phi'). \tag{41}$$

for $r \gg r_s$. Here $C_1(\phi')$ is a function of ϕ' which comes out due to the integration over r'.

We assume B'_ϕ is constant along longitudinal (ϕ') direction within a streamtube (Figure 1), that is, $\partial B'_\phi/\partial\phi' = 0$ either for all ϕ' or locally, for a limited range of ϕ' (Tasnim & Cairns, 2016). This assumption allows us to reduce (16) to the form $(1/r'^2)d(r'^2 B'_r)/dr' = 0$. Integrating Gauss's Law over r' yields

$$r'^2 B'_r(r', \phi') = C_2(\phi'), \tag{42}$$

where $C_2(\phi')$ is a function of ϕ'.

Similarly, Faraday's Law (27) with the assumption $\partial B'_\phi/\partial\phi'$ in the corotating frame reduces to

$$\frac{1}{r'}\frac{\partial}{\partial r'}\left[r'(-v'_r B'_\phi + v'_\phi B'_r + \Omega r' B'_r)\right] = 0. \tag{43}$$

Integrating (43) over r' results in

$$r'[v'_r(r', \phi')B'_\phi(r', \phi') - v'_\phi(r', \phi)B'_r(r', \phi')] = C_3(\phi'), \tag{44}$$

where $C_3(\phi')$ is a function of ϕ'. Since $C_3(\phi')$ can be nonzero in principle, (44) is more general than the assumption $C_3(\phi') = 0$ that corresponds to $\mathbf{v}'$ and $\mathbf{B}'$ being parallel in the rotating frame.

We assume that ρ', v'_ϕ, and B'_ϕ are constant either for all ϕ' or locally, for a limited range of ϕ' where $\partial\rho'/\partial\phi'$, $\partial v'_\phi/\partial\phi'$, and $\partial B'_\phi/\partial\phi'$ can be neglected. After integrating over r' and using the above assumptions, the θ component of (31) gives

$$r'v'_\phi(r', \phi') + r'\Omega - \frac{r'B'_r(r', \phi')B'_\phi(r', \phi')}{\mu_0\rho'(r', \phi')v'_r(r', \phi')} = L'_\theta(\phi'), \tag{45}$$

where for $\theta = 90°$, $L'_\theta(\phi') = L'_z(\phi')$, assuming $v'_\theta = 0$ and $B_\theta = 0$. The first term of (45) represents the standard unmagnetized fluid angular momentum per unit mass density, the second term $r'\Omega$ presents angular momentum due to torque associated with the coriolis force in the rotating frame, and the third term represents the magnetic field contribution. The sum of these terms must be a function of ϕ', and be equal to the total out-of-plane angular momentum ($\mathbf{L}' = L'_z(r', \phi')\mathbf{e}_z$) carried away from the Sun per unit mass density. Note that the ϕ' component of $\mathbf{L}'$ (i.e., $L'_\phi\mathbf{e}_\phi$) analogous to (45) depends on v'_θ and the product $B'_r B'_\theta$, both of which are zero by assumption, so that $L'_\phi = 0$. Likewise $L'_r = 0$.

In the inertial frame, after integrating over r, the θ component of (30) with the assumption $\partial L_{\star\theta}/\partial t = \partial L_{\star z}/\partial t = 0$ becomes

$$rv_\phi(r, \phi, t) - \frac{rB_r(r, \phi, t)B_\phi(r, \phi, t)}{\mu_0\rho(r, \phi, t)v_r(r, \phi, t)} = L_\theta(\phi, t) = L_z(\phi, t), \tag{46}$$

The integration constants in (41), (42), (44), and (45) are found by applying boundary conditions at the inner boundary (r'_s, ϕ'_s) of the solar wind, where the magnetic field components are $B'_r(r'_s, \phi'_s)$ and $B'_\phi(r'_s, \phi'_s)$, and the velocity components are $v'_r(r'_s, \phi'_s)$ and $v'_\phi(r'_s, \phi'_s)$. The total azimuthal velocity at the inner boundary is written

as $v'_\phi(r'_s, \phi'_s) = \delta v'_\phi(r_s, \phi_s)$, where $\delta v'_\phi(r'_s, \phi'_s)$ represents a deviation from corotation [$\delta v'_\phi(r'_s, \phi'_s) = \delta v_\phi(r, \phi, t)$].
Equations (41), (42), (44), and (45) then become

$$r' \left[v'_r(r', \phi')B'_\phi(r', \phi') - (v'_\phi(r', \phi') + \Omega r')B'_r(r', \phi') \right]$$
$$= r'_s \left[v'_r(r'_s, \phi'_s)B'_\phi(r'_s, \phi'_s) - \delta v'_\phi(r'_s, \phi'_s)B'_r(r'_s, \phi'_s) - \Omega r'_s B'_r(r'_s, \phi'_s) \right], \tag{47}$$

and

$$r'^2 B'_r(r', \phi') = r_s'^2 B'_r(r'_s, \phi'_s), \tag{48}$$

$$\rho'(r', \phi')r'^2 v'_r(r', \phi') = \rho'(r'_s, \phi'_s)r_s'^2 v'_r(r'_s, \phi'_s), \tag{49}$$

$$r'v'_\phi(r', \phi') + r'^2\Omega - \frac{r'B'_r(r', \phi')B'_\phi(r', \phi')}{\mu_0 \rho'(r', \phi')v'_r(r', \phi')}$$
$$= r'_s[r'_s\Omega + \delta v'_\phi(r'_s, \phi'_s)] - \frac{r'_s B'_r(r'_s, \phi'_s)B'_\phi(r'_s, \phi'_s)}{\mu_0 \rho'(r'_s, \phi'_s)v'_r(r'_s, \phi'_s)}. \tag{50}$$

An expression for $v_\phi(r, \phi)$ is found by solving (50) and (47) simultaneously:

$$v'_\phi(r', \phi') = \frac{d_1}{[1 - M_A'^2(r', \phi')]} \times \left[1 - M_A'^2(r', \phi')\frac{d_2}{d_1} \right], \tag{51}$$

where $M_A'^2(r', \phi') = \mu_0\rho'(r', \phi')v_r'^2(r', \phi')/B_r'^2(r', \phi') = v'_r(r', \phi')r'^2/[v'_a(r'_A)r_A'^2(\phi'_a)]$, and

$$d_1 = r'\Omega - \frac{r'_s v'_r(r'_s, \phi'_s)B'_\phi(r'_s, \phi'_s)}{r'B'_r(', \phi')} + \frac{r'_s \delta v'_\phi(\phi'_s)B_r(r'_s, \phi'_s)}{r'B'_r(r', \phi')},$$

$$d_2 = \frac{r_s'^2\Omega}{r'} + \frac{r'_s\delta v'_\phi(\phi'_s)}{r'} - \frac{r'_s B'_r(r'_s, \phi'_s)B'_\phi(r'_s, \phi'_s)}{\mu_0\rho'_s(\phi'_s)v'_r(r'_s, \phi'_s)r'} - r'\Omega.$$

This is similar to the approach of Weber and Davis (1967). In section 4 below, we use this expression for $v'_\phi(r', \phi')$ to derive $B'_\phi(r', \phi')$ as a function of r'.

A singularity problem arises in (51) at the Alfvénic critical radius where the radial Alfvénic Mach number $M'_A(r'_A, \phi'_a) = 1$. To remove the singularity at the Alfvénic critical radius $r'_A(\phi'_a)$ the denominator and numerator must both vanish at $r' = r'_A$ and $\phi' = \phi'_a$ (Weber & Davis, 1967), requiring

$$\frac{r_s'^2\Omega}{r'_A(\phi'_a)} + \frac{r'_s\delta v'_\phi(r'_s, \phi'_s)}{r'_A(\phi'_s)} - \frac{r'_s B'_r(r'_s, \phi'_s)B'_\phi(r'_s, \phi'_s)}{\mu_0\rho'(r'_s, \phi'_s)v'_r(r'_s, \phi'_s)r'_A(\phi'_a)} - r'_A\Omega$$
$$= r'_A(\phi'_a)\Omega - \frac{r'_s}{r'_A(\phi'_a)B'_r(r'_A, \phi'_a)} \left[v'_r(r'_s, \phi'_s)B'_\phi(r'_s, \phi'_s) - \delta v'_\phi(r'_s, \phi'_s)B'_r(r'_s, \phi'_s) \right]. \tag{52}$$

4. Analytic Results

This section presents analytic solutions to the equations in section 3 that are amenable to fitting with spacecraft data. We start with predictions for the inner boundary, then proceed to the radial profile $v'_r(r', \phi'_{ob})$, and then present results for all (r', ϕ'). Note that we use (1)–(7) to relate the spacecraft observations in an inertial frame to the variables in the rotating frame. For example, $\rho'(r', \phi'_{ob}) = \rho(r, \phi_{ob}, t_{ob})$, $v'_r(r', \phi'_{ob}) = v_r(r, \phi_{ob}, t_{ob})$, $v'_\phi(r'_{ob}, \phi'_{ob}) = v_\phi(r, \phi_{ob}, t_{ob}) + \Omega r_{ob}$, $B'_r(r', \phi'_{ob}) = B_r(r, \phi_{ob}, t_{ob})$, and $B'_\phi(r', \phi'_{ob}) = B_\phi(r, \phi_{ob}, t_{ob})$.

4.1. Extraction of the Intrinsic $B_\phi(r_s, \phi_s)$ and $v_\phi(r_s, \phi_s)$
We allow intrinsic magnetic field components $B'_r(r'_s, \phi'_s)$ and $B'_\phi(r'_s, \phi'_s)$ at the inner boundary (r'_s, ϕ'_s). Simultaneous use of (52)–(47) with the application of observations at specific locations $r = r_{ob}$ and $\phi = \phi_{ob}$ allow us to derive the following expressions for $B'_r(r'_s, \phi'_s)$, $v'_\phi(r'_s, \phi'_s)$, $\delta v'_\phi(r'_s, \phi'_s)$, and $B'_\phi(r'_s, \phi'_s)$:

$$B_r(r_s, \phi_s, t_s) = B'_r(r'_s, \phi'_s) = \frac{r_{ob}'^2}{r_s'^2}B'_r(r'_{ob}, \phi'_{ob}), \tag{53}$$

$$
\delta v_\phi(r_s, \phi_s, t_s) = \delta v'_\phi(r'_s, \phi'_s) = \left[r'_s\Omega - \frac{r'^2_A(\phi'_a)\Omega}{r'_s} \right] \left[\frac{1}{M'^2_A(r'_s, \phi'_s) - 1} \right]^{-1}
$$
$$
+ d_3 \left[\frac{r'v'_r(r'_{ob}, \phi'_{ob})B'_\phi(r'_{ob}, \phi'_{ob})}{r'_s B'_r(r'_{ob}, \phi'_{ob})} - \frac{r'v'_\phi(r'_{ob}, \phi'_{ob})}{r'_s} + \frac{\Omega r'}{r'_s} \right],
\tag{54}
$$

$$
v'_\phi(r'_s, \phi'_s) = \delta v'_\phi(r'_s, \phi'_s),
\tag{55}
$$

$$
v_\phi(r_s, \phi_s, t_s) = v'_\phi(r'_s, \phi'_s) + r_s\Omega = \delta v'_\phi(r'_s, \phi'_s) + r_s\Omega,
\tag{56}
$$

$$
B_\phi(r_s, \phi_s, t_s) = B'_\phi(r'_s, \phi'_s) = \frac{r'v'_r(r'_{ob}, \phi'_{ob})B'_\phi(r'_{ob}, \phi'_{ob})}{r'_s v'_r(r'_s, \phi'_s)} - \frac{r'_{ob}v'_\phi(r'_{ob}, \phi'_{ob})B'_r(r'_{ob}, \phi'_{ob})}{r'_s v'_r(r'_s, \phi'_s)}
$$
$$
+ \frac{\delta v'_\phi(r'_s, \phi'_s)B'_r(r'_s, \phi'_s)}{v'_r(r'_s, \phi'_s)} + \frac{\Omega r'^2_s B_r(r'_s, \phi'_s)}{r'_s v'_r(r_s, \phi_s)},
\tag{57}
$$

where

$$
d_3 = \frac{r'^2_A(\phi_a)}{r'^2} \left[M'^2_A(r'_s, \phi'_s) - \frac{r'^2_s}{r'^2_A} \right] \left[1 - M'^2_A(r'_s, \phi'_s) \right]^{-1},
$$

and

$$
M_A(r_s, \phi_s, t_s) = M'_A(r'_s, \phi_{s'}) = \frac{\mu_0\rho'(r'_s, \phi'_s)v'^2_r(r'_s, \phi'_s)}{B'^2_r(r'_s, \phi'_s)}.
\tag{58}
$$

The corresponding prediction for $v_\phi(r'_{ob}, \phi'_{ob})$ from (51) is

$$
v_\phi(r'_{ob}, \phi'_{ob}) = \left[1 - \frac{r'^2_A}{r'^2} \right]^{-1} \left[\frac{2\Omega r'^2_A}{r'} - 2\Omega r' \right]
$$
$$
+ \left[\frac{r'^2_{ob}}{r'^2_A(\phi'_a)} - 1 \right]^{-1} \left[\frac{r'^2_{ob}}{M'^2_A(r'_{ob}, \phi'_{ob})r'^2_A(\phi'_a)} - 1 \right] \left[\frac{v'_r(r'_{ob}, \phi'_{ob})}{B'_r(r'_{ob}, \phi'_{ob})} \right] B'_\phi(r', \phi').
\tag{59}
$$

where

$$
M_A(r_{ob}, \phi_{ob}, t_{ob}) = M'_A(r'_{ob}, \phi'_{ob}) = \frac{\mu_0\rho'(r'_{ob}, \phi'_{ob})v'^2_r(r'_{ob}, \phi'_{ob})}{B'^2_r(r'_{ob}, \phi'_{ob})}.
\tag{60}
$$

4.2. Solution for $v'_r(r', \phi'_{ob}) = v_r(r, \phi_{ob}, t_{ob})$

We solve Parker's isothermal wind model using an implicit method. The boundary restriction $v'_r(r', \phi'_{ob}) = v_r(r, \phi_{ob}, t_{ob}) = c'_s(\phi'_{ob}) = c_s(\phi_{ob}, t_{ob})$ at $r = r_{so}$ yields the appropriate integration constant of (36) as $C_5(\phi'_{ob}) = -3$. We assume a reasonable value for the sonic critical radius, $r'_{so}(\phi'_{ob}) = 5R_\odot$, where the radial flow speed $v'_r(r'_{so}, \phi'_{ob}) = c'_s(\phi'_{ob})$. An isothermal wind of ionized hydrogen has constant sound speed,

$$
c'_s(\phi'_{ob}) = c_s(\phi_{ob}, t_{ob}) = \left[\frac{2k_B T'_{iso}(\phi'_{ob})}{m_i} \right]^{1/2},
\tag{61}
$$

or alternatively

$$
T'_{iso}(\phi'_{ob}) = T_{iso}(\phi_{ob}, t_{ob}) = \frac{c'^2_s(\phi)m_i}{2k_B}.
\tag{62}
$$

Similarly, we solve for $v'_r(r', \phi_{ob})$ for a particular ϕ_{ob}, where $C_5(\phi'_{ob}) = C_5(\phi_{ob}, t_{ob}) = -3$. Figure 2 (black line) shows the radial variation of $v'_r(r', \phi'_{ob}) = v_r(r, \phi_{ob}, t_{ob})$ and the right-hand axis shows the value of $v_r(r, \phi_{ob}, t_{ob})/c_s(\phi_{ob}, t_{ob})$. The heliocentric distance 1 AU can be written as $r \approx 215R_\odot \approx 43r_{so} = 43r_{so}$ $(r_{so} = r'_{so})$. Figure 2 shows that the predicted radial solar wind speed at 1 AU is

$$
v_r(r, \phi_{ob}, t_{ob}) = v'_r(r', \phi') = v_r(1 \text{ AU}, \phi_{ob}, t_{ob}) = 3.85\, c_s(\phi_{ob}, t_{ob}) = 3.85\, c'_s(\phi'_{ob}).
\tag{63}
$$

In section 5 below we fit the predicted solution (63) to the observed $v'_r(1 \text{ AU}', \phi'_{ob})$ data from the Wind spacecraft and so obtain $c'_s(\phi') = c_s(\phi, t)$ and $T'_{iso}(\phi') = T_{iso}(\phi, t)$ as a function ϕ'_{ob} for the period 1 to 27 August 2010.
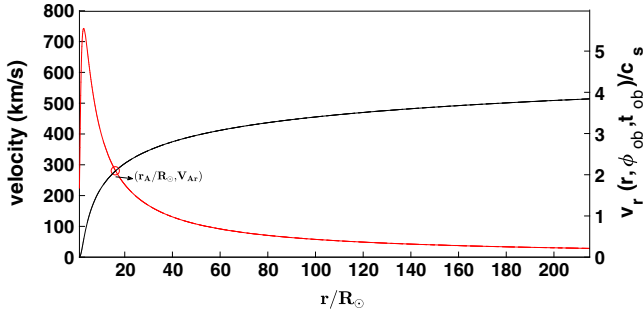
Figure 2. Radial velocity $v_r(r, \phi_{ob}, t_{ob}) = v'_r(r', \phi'_{ob})$ solution for an isothermal accelerating solar wind (black) and radial variation of the radial Alfvén speed $V_{Ar}(r) = V_{Ar'}(r')$ (red). The left y axis shows speeds in km s^{-1}, obtained using 1 AU data for a given phase angle ϕ [$\phi_{ob} = \phi_{ob}(t_{ob} = 1$ h)] and corresponding values of v_r(1 AU). The curves intersect at the Alfvén critical radius ($r_A' = r_A$). The right y axis represents $v_r(r, \phi_{ob}, t_{ob})/c_s$ as a function of $r/R_\odot$, where c_s is the sound speed.

4.3. Radial Profiles of $n'(r', \phi')$, $B'_r(r', \phi')$, $v'_\phi(r', \phi')$, and $B'_\phi(r', \phi')$
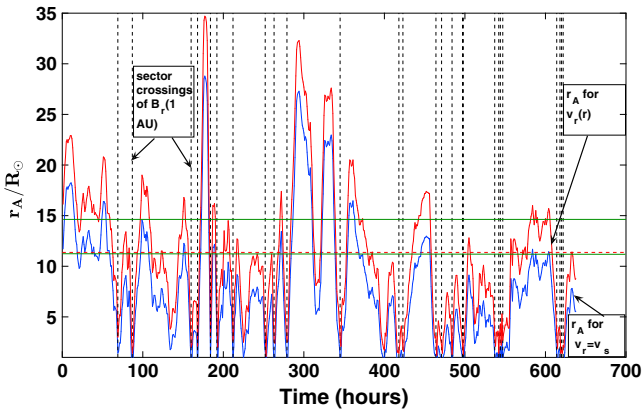
The mass conservation equation (41) yields

$$n(r, \phi_{ob}, t_{ob}) = n'(r', \phi'_{ob}) = \frac{n'(r'_{ob}, \phi'_{ob})v'_r(r'_{ob}, \phi'_{ob})r'^2_{ob}}{r'^2 v'_r(r', \phi')}. \tag{64}$$

Similarly, the flux conservation equation (42) gives

$$B_r(r, \phi_{ob}, t_{ob}) = B'_r(r', \phi'_{ob}) = \frac{r_{ob}'^2 B'_r(r'_{ob}, \phi'_{ob})}{r'^2}. \tag{65}$$

We obtain an analytic expression for $v'_\phi(r', \phi'_{ob})$ as a function of r' by combining (48)–(50), yielding

$$v_\phi(r, \phi_{ob}, t_{ob}) - \Omega r = v'_\phi(r', \phi'_{ob}) = \frac{q_1}{[1 - M'^2_A(r', \phi'_{ob})]}\left[1 - M'^2_A(r', \phi'_{ob})\frac{q_2}{q_1}\right], \tag{66}$$

where

$$q_1 = r'\Omega - \frac{r'r'_s}{r'^2_{ob}B'_r(r'_{ob}, \phi'_{ob})}\left[v'_r(r'_s, \phi'_s)B'_\phi(r'_s, \phi'_s) - \delta v'_\phi(r'_s, \phi'_s)B'_r(r'_s, \phi'_s)\right],$$

$$q_2 = \frac{r'^2_s\Omega}{r'} - r'\Omega + \frac{r'_s\delta v'_\phi(r'_s, \phi'_s)}{r'} - \frac{r'_s B'_r(r'_s, \phi'_s)B'_\phi(r'_s, \phi'_s)}{\mu_0\rho'(r'_s, \phi'_s)v'_r(r'_s, \phi'_s)r'}.$$

By using (48), (49), (47), and the results from (66), we obtain the radial variation of $B'_\phi(r', \phi'_{ob})$:

$$\begin{aligned} B_\phi(r, \phi_{ob}, t_{ob}) = B'_\phi(r', \phi'_{ob}) = \frac{r'_s v'_r(r'_s, \phi'_s)B'_\phi(r'_s, \phi'_s)}{r'v'_r(r', \phi'_{ob})} - \frac{r'_s\delta v'_\phi(r'_s, \phi'_s)B'_r(r'_s, \phi'_s)}{r'v'_r(r', \phi'_{ob})} \\ + \frac{v'_\phi(r', \phi')r'^2_{ob}B'_r(r'_{ob}, \phi'_{ob})}{r'^3 v'_r(r', \phi'_{ob})} - \frac{\Omega r'^2_s B'_r(r'_s, \phi'_s)}{r'v'_r(r', \phi'_{ob})}. \end{aligned} \tag{67}$$

5. Applications of the Data-Driven Model

We demonstrate the new accelerating solar wind model for the solar rotation from 1 to 27 August 2010. The corresponding hourly data from the Wind spacecraft (Farrell et al., 1995; Leinweber et al., 2008; Lepping et al., 1995) are shown in Appendix A (Figure A1) for the period of interest — more details are provided in Tasnim and Cairns (2016). We combine these 1 AU data from the Wind spacecraft for $B_r(r_{ob}, \phi_{ob}, t_{ob})$, $B_\phi(r_{ob}, \phi_{ob}, t_{ob})$, $v_r(r_{ob}, \phi_{ob}, t_{ob})$, $n_i(r_{ob}, \phi_{ob}, t_{ob})$, and $T_i(r_{ob}, \phi_{ob}, t_{ob})$ at each specific $(r_{ob}, \phi_{ob}, t_{ob})$ with the radial solution for $v'_r(r', \phi')$ and (53)–(59) to find c'_s, $r'_A(\phi'_a)$, $B'_r(r'_s, \phi'_s)$, $\delta v'_\phi(r'_s, \phi'_s)$, $v'_\phi(r'_s, \phi'_s)$, $B'_\phi(r'_s, \phi'_s)$, and v'_ϕ(1 AU$'$), as described in section 4. Then we apply (64)–(66), and (67) to predict the radial profiles of $v'_\phi(r', \phi')$ and $B'_\phi(r', \phi')$. Subsequently, we predict **L**$'$ (i.e., $L'_z(\phi') = L'_\theta(\phi')$), $E'_z = E'_\theta$, and the power law index γ of the temperature profile (we explain later in section 5.6) from the 1 AU data. We reduce the variabilities in the observations using a centered boxcar average of the 1 h data over 11 h. Since most of the turbulence is usually on timescales of less than 10 h, the 11 h averaging smooths out turbulence in the observations.

5.1. Alfvénic Radius r_A and the Alfvén Surface

The radial Alfvén speed $V_{Ar} = V_{Ar'}$ is defined as a function of r' and ϕ' by

$$V_{Ar}(r, \phi, t) = V'_{Ar}(r', \phi') = \frac{r'B'_r(r', \phi')\sqrt{v'_r(r', \phi')}}{r'_{ob}\sqrt{\mu_0\rho'(r'_{ob}, \phi'_{ob})v'_r(r'_{ob}, \phi'_{ob})}}, \tag{68}$$

which is calculated using the previous equations (64) and (65), the observed values of $B'_r(r'_{ob}, \phi'_{ob}) = B_r(r_{ob}, \phi_{ob}, t_{ob})$, $v'_r(r'_{ob}, \phi'_{ob}) = v_r(r_{ob}, \phi_{ob}, t_{ob})$, and $\rho'(r'_{ob}, \phi'_{ob}) = \rho(r_{ob}, \phi_{ob}, t_{ob})$, the assumed sonic radius $r'_{so} = r_{so}$, and the corresponding acoustic speed $c_s(\phi_{so}, t_{so}) = c'_s(\phi'_{so})$ at $r_{so} = r'_{so}$ for a solar period. Figure 2 shows results for $v_r(r, \phi_{ob}, t_{ob}) = v'_r(r', \phi'_{ob})$ and $V_{Ar}(r, \phi_{ob}, t_{ob}) = V'_{Ar}(r', \phi'_{ob})$ based on the data for the period of 1 to 27 August 2010. The intersection of the radial profiles yields $r_a(\phi_a, t_a) = r'_A(\phi'_a)$ for a given phase

Figure 3. Time variations of $r_A = r_A'$ along the Earth-Sun line for the period 1–27 August 2010. The red line shows r_A for the accelerating wind model ($r_s = r_s' = R_\odot$), whereas the blue line is for the constant speed model (Tasnim & Cairns, 2016). Green solid lines show the lower limits for the Alfvén surface (more properly the fast mode surface): $15\,R_\odot$ over the steamer belt and $12\,R_\odot$ over a coronal hole (DeForest et al., 2014). The broken red line shows the mean of r_A predicted using the accelerating wind model.

angle $\phi_{ob}' = \phi_{ob} - \Omega t$. Consequently, predictions for $r_A(\phi_a, t_a) = r_A'(\phi_a')$ are made from the intersections of $V_{Ar}(r, \phi, t) = V_{Ar}'(r', \phi')$ and $v_r(r, \phi, t) = v_r'(r', \phi')$ for the full solar period (Figure 3) of 1 to 27 August 2010. Figure 3 (red line) shows that the predicted values of $r_A(\phi_a, t_a) = r_A'(\phi_a')$ for the accelerating wind model vary between $5R_\odot$ and $35R_\odot$ with an average of $\approx 12R_\odot$. This average value is very close to the estimated values of r_A above coronal holes (DeForest et al., 2014).

Strong time, hence variations as a function of $\phi' = \phi - \Omega t$, variations in r_A are evident in Figure 3. These variations are driven by the solar wind data at 1 AU and so are due physically to intrinsic changes in the coronal parameters at the inner boundary on both short and long scales. The variations in $\phi' = \phi - \Omega t$ are not unexpected since most SDO, SOHO, STEREO, and other solar images show strong longitudinal variations in coronal and disk structures and features, such as active regions and magnetic loops. Figure 3 also shows that very small values of $r_A \leq 5R_\odot$ typically correspond to sector crossings at 1 AU (vertical black lines) where $B_r'(r_{ob}', \phi_{ob}') = B_r(r_{ob}, \phi_{ob}, t_{ob})$ has a small magnitude. The new predictions for $r_A'(\phi_a') = r_A(\phi_a, t_{ob})$ are similar to the values of $r_A'(\phi_a')$ predicted for the constant $v_r = v_r'$ wind model (blue line) of Tasnim and Cairns (2016), being displaced outward to larger r by an approximately constant distance of $\gtrsim 1\,R_\odot$. This is consistent with $r_A'(\phi_a') = r_A(\phi_a, t_a)$ being driven primarily by the values of B_r' and n' at 1 AU and not by $v_r' = v_r$. An interpretation is that the accelerating solar wind is slow at small r and so has to travel further out than to meet the condition that $v_r(r, \phi, t) = v_r'(r', \phi') = V_{Ar}'(r', \phi') = V_{Ar}(r, \phi, t)$ in the case the wind speed is constant at all $r = r'$.

5.2. Extraction of Intrinsic $B_\phi(r_s, \phi_s, t_s)$ and $v_\phi(r_s, \phi_s, t_s)$

The new model allows a deviation δv_ϕ from corotation in the azimuthal velocity $v_\phi(r_s, \phi_s, t_s)$ at the inner boundary. Figure 4 shows the predictions for $\delta v_\phi(r_s, \phi_s, t_s)$ for the period studied.

The predicted values of $\delta v_\phi(r_s, \phi_s, t_s)$ typically vary between $-20\ \text{km s}^{-1}$ and $20\ \text{km s}^{-1}$ with a mean of $-0.8\ \text{km s}^{-1}$ for $r_s = R_\odot$. Figure 4 shows that very large values of $|\delta v_\phi(r_s, \phi_s, t_s)|$ ($\gtrsim 20\ \text{km s}^{-1}$) are mostly apparent at the sector crossings of $B_r(1\ \text{AU}, \phi_{ob}, t_{ob})$, where $B_r(1\ \text{AU}, \phi_{ob}, t_{ob})$ is small in magnitude. Note that sector crossings are shown by the vertical black lines. The analytic expression (54) also shows that small values of $B_r(r_{ob}, \phi_{ob}, t_{ob})$ lead to $\delta v_\phi(r_s, \phi_s, t_s)$ being large. We consider now times when $|\delta v_\phi(r_s, \phi_s, t_s)| \leq 20\ \text{km s}^{-1}$, so as to avoid very large values of $\delta v_\phi(r_s, \phi_s, t_s)$, corresponding to the sector crossings of $B_r(1\text{AU}, \phi_{ob}, t_s)$.
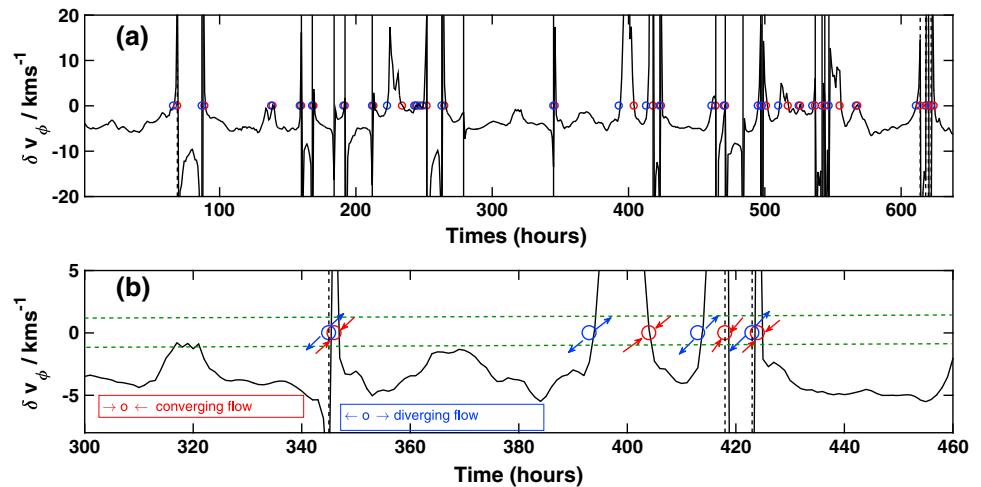
Figure 4. Variation of $\delta v_\phi(r_s, \phi_s, t_s) = \delta v_\phi'(r_s', \phi_s')$ with time t for the period 1–27 August 2010 for $r_s = r_s' = R_\odot$. Positive δv_ϕ means the deviation from corotation is in the corotation direction, while negative δv_ϕ means a direction opposite to corotation. Changes from positive to negative δv_ϕ represent converging flows, whereas changes from negative to positive represent diverging flows. Here green lines show the thresholds ($\pm 1\ \text{km s}^{-1}$) used to identify changes in the flow pattern.
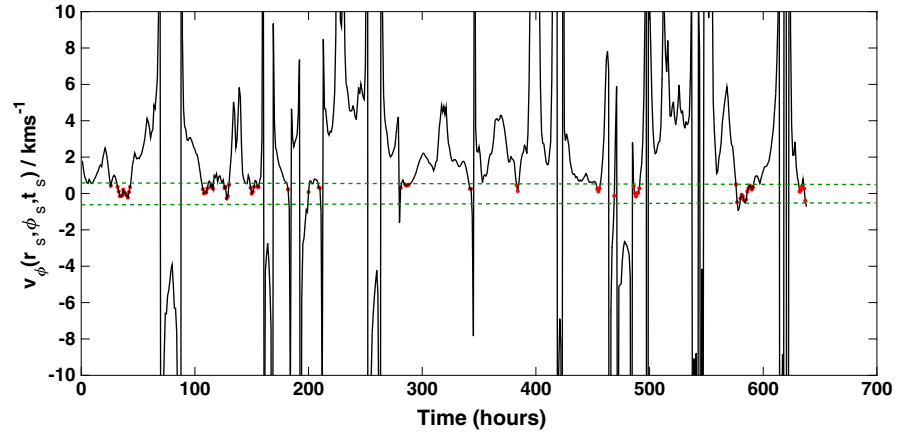
Figure 5. Variation of $v_\phi(r_s, \phi_s, t_s) = v'_\phi(r'_s, \phi'_s) + r_s\Omega$ with time t for the period 1–27 August 2010 for $r_s = r'_s = R_\odot$. Red (circles) markers display the points where $v_\phi(r_s, \phi_s, t) \simeq 0$. The values of $v_\phi(r_s, \phi_s, t_s)$ have two contributions: one due to the corotation ($r_s\Omega$) and the other due to the deviation from corotation (δv_ϕ). Green lines show the limits (± 0.5 km s^{-1}) within which $v_\phi(r_s, \phi_s, t_s)$ is considered small enough to be approximately zero in comparison with the radial speed. Values $v_\phi(r_s, \phi_s, t_s) \simeq 0$ occur when the effects of corotation ($r_s\Omega$) are canceled by the effects of δv_ϕ; that is, where $\delta v_\phi \simeq -r_s\Omega$.

Sign changes of $\delta v_\phi(r_s, \phi_s, t_s)$ are evident at the sector crossings of $B_r(1 \text{ AU}, \phi_{ob}, t_{ob})$. Positive $\delta v_\phi(r_s, \phi_s, t_{ob})$ corresponds to the corotation direction, with negative $\delta v_\phi(r_s, \phi_s, t_{ob})$ values directed oppositely. Inspecting the data, $\delta v_\phi(r_s, \phi_s, t_s)$ changes sign on average of every 10 h, with a maximum timescale of 40 h and minimum timescale of 1 h. Pairs of inward directed arrows in Figure 4 represent two azimuthal flows heading toward each other. Ideally, these converging flows will compress the plasma and so increase the local plasma density. On the other hand, pairs of outward directed arrows show where the azimuthal flows are departing from each other, forming a diverging flow region and so on. These diverging flows ideally form a rarefaction in the plasma and a decrease in the local plasma density. Turbulence can affect the interpretation. Hence, we define a threshold velocity of ± 1 km s^{-1} to robustly identify flow patterns. Figure 4b shows such regions.

Granulation and supergranulation convection cells naturally have converging and diverging flow patterns in the azimuthal and polar directions. Therefore, we interpret the model predictions for converging and diverging flow patterns in $\delta v_\phi(r_s, \phi_s, t_{ob})$ in terms of the boundaries and centers, respectively, of these convective cells. These flows thus are signatures in the wind plasma of the convective cells and should have the spatiotemporal characteristics (Jokipii & Parker, 1968). These association are discussed in section 6.

Figure 5 shows another aspect of the $v_\phi(r_s, \phi_s, t_s)$ predictions, focusing on where the deviation from corotation is strong enough to overcome the corotation, leading to an approximately radial outflow from the inner boundary, that is, $v_\phi(r_s, \phi_s, t_s) \simeq 0$. The red (o) markers denote the points when $\delta v_\phi(r_s, \phi_s, t_s) \simeq -r_s\Omega$. At these points, the intrinsic nonradial velocity $\delta v_\phi(r_s, \phi_s, t_s)$ is significant relative to the corotation velocity and can even dominate corotation. Put another way, at these locations the predicted deviations δv_ϕ from corotation are significant.

Figure 6 displays how the predicted values of $v_\phi(r_s, \phi_s, t_s)$ change for different choices of r_s. Clearly the variations with ϕ are similar for the different values of r_s, with only the magnitude changing: the magnitudes rise from $r_s = R_\odot$ to $5R_\odot$ but then decrease to much lower values at 1 AU. For $r_s = R_\odot$ the mean value of $v_\phi(r_s, \phi_s, t_s)$ is very close to the corotation speed, but at $5R_\odot$ the mean value of v_ϕ is well below the corotation speed, decreasing even more at large r. Thus, the model fits show that the assumption of mean corotation is viable only if r_s is close to $R_\odot$.

The large values of $v_\phi(r_s, \phi_s, t_s)$ in Figure 6 tend to occur at sector crossings (vertical black lines) where $B_r(r_{ob}, \phi_{ob}, t_{ob})$ is small. The analytic expression (55) shows that for each assumed r_s, the value of $v_\phi(r_s, \phi_s, t_s)$ varies with $\delta v_\phi(r_s, \phi_s, t_s)$. Since $\delta v_\phi(r_s, \phi_s, t_s)$ has large magnitudes compared with the corotation velocity at the sector crossings, small values of $B_r(r_{ob}, \phi_{ob}, t_{ob})$ lead to $v_\phi(r_s, \phi_s, t_s)$ becoming large. Small values
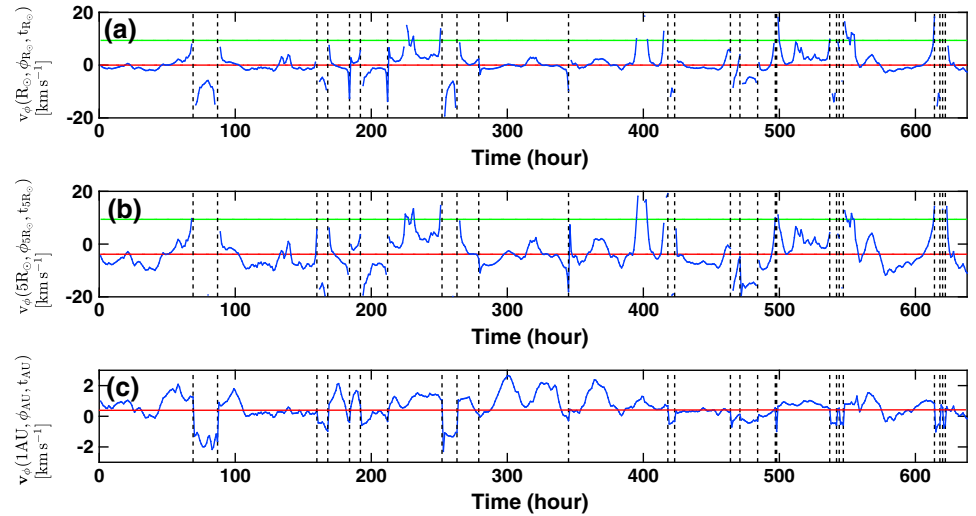
Figure 6. Time (ϕ) variations of predictions for $v_\phi(r_s, \phi_s, t_s) = v_\phi(r_s', \phi_s') + r_s\Omega$ with (a) $r_s = R_\odot$, (b) $r_s = 5R_\odot$, and (c) the predictions for $v_\phi(1\,\text{AU}, \phi_{ob}, t_{ob})$ with $r_s = 5R_\odot$. Horizontal green lines show the corotation speed $r_s\Omega$, whereas red lines show the mean of the new model's predictions (excluding samples with $|v_\phi(r_s, \phi_s, t_s)| > 20$ km s^{-1}). Vertical black lines represent the sector crossings of $B_r(1\,\text{AU}, \phi_{AU}, t_{AU})$. Note that positive values correspond to v_ϕ being directed in the corotation direction and negative values correspond to v_ϕ being oppositely directed.

of $B_r(r_{ob}, \phi_{ob})$ also significantly change other predicted quantities near sector crossings, for example, $r_A(\phi_a)$, $\delta v_\phi(r_s, \phi_s, t_s)$, and $B_\phi(r_s, \phi_s, t_s)$. These abrupt changes in the predicted solar wind quantities near sector boundaries in B_r correspond to where the model breaks down, since $\partial/\partial\phi$ variations should not be neglected in (44), (42), and (45).

Figure 6c displays the predicted variations in v_ϕ at 1 AU when $r_s = R_\odot$. The statistical mean is $\simeq 0.5$ km s^{-1} which is much smaller than the predicted mean of $v_\phi(1\,\text{AU}) \simeq 7.1$ km s^{-1} from the Tasnim and Cairns (2016) model, and the new predicted values of $v_\phi(1\,\text{AU})$ are sometimes antiparallel to corotation, not only in the corotation direction. These differences at the inner boundary are primarily due to the new model permitting a deviation from corotation at the inner boundary, which is clearly a quantitatively important generalization. The smaller value of $v_\phi(1\,\text{AU})$ in comparison with the radial speed $v_r(1\,\text{AU})$ demonstrates that the solar wind comes out almost radially, similar to Parker's model (Parker, 1958).

Figure 7 compares the azimuthal field predicted at (r_s, ϕ_s, t_s) by the new model, $|B_{\phi 1}(r_s, \phi_s, t_{ob})|$, with the field $B_{\phi 2}(r_s, \phi_s, t_s)$ predicted for the constant speed wind model (Schulte in den Bäumen et al., 2011, 2012). Quantitatively important differences are evident. The values of $B_{\phi 1}(r_s, \phi_s, t_s)$ for the accelerating wind model are in the range $10^{-7} T - 10^{-5} T$, whereas the values of $B_{\phi 2}(r_s, \phi_s, t_s)$ for the constant speed wind model lie in the range $10^{-8} T - 10^{-6} T$. The averages of the ratio between the intrinsic azimuthal field components for the two models are $\langle B_{\phi 1}/B_{\phi 2} \rangle \simeq -3.6$ and $\langle |B_{\phi 1}/B_{\phi 2}| \rangle \simeq 42.5$. Note that $B_\phi(r_s, \phi_s, t_s)$ from the Schulte in den Bäumen et al. (2011, 2012) model is

$$B_\phi(r_s, \phi_s, t_s) = \left[B_\phi(r_{ob}, \phi_{ob}, t_{ob}) + B_r(r_{ob}, \phi_{ob}, t_{ob})\frac{(r_{ob} - r_s)\Omega_s \sin\theta_{ob}}{v_s} \right] \frac{r_{ob}}{r_s}, \qquad (69)$$

where v_s is the constant radial wind speed. An interpretation for $B_{\phi 1}$ typically exceeding $B_{\phi 2}$ in magnitude involves v_s in the replacement of $v_r(r, \phi_{ob}, t_{ob})$ in the denominator of (57) and (69). Note that $v_r(r, \phi_{ob}, t_{ob})$ increases with r in the accelerating wind model to the 1 AU value, whereas the constant speed model uses $v_r(r, \phi_{ob}, t_{ob}) = v_s = v_r(1\,\text{AU})$ for all radial distance r. Thus, at small r where $v_r(r, \phi_{ob}, t_{ob})$ is small, $|B_{\phi 1}|$ should be larger than $|B_{\phi 2}|$. Indeed, typically $|B_{\phi 1}| \geq |B_{\phi 2}|$, although both $B_{\phi 1}$ and $B_{\phi 2}$ vary with time by more than an order of magnitude.

In the constant v_r model of Schulte in den Bäumen et al. (2011, 2012), the intrinsic $B_\phi(r_s, \phi_s, t_s)$ values are interpreted in terms of granulation and supergranulation cells moving the field lines, despite assuming
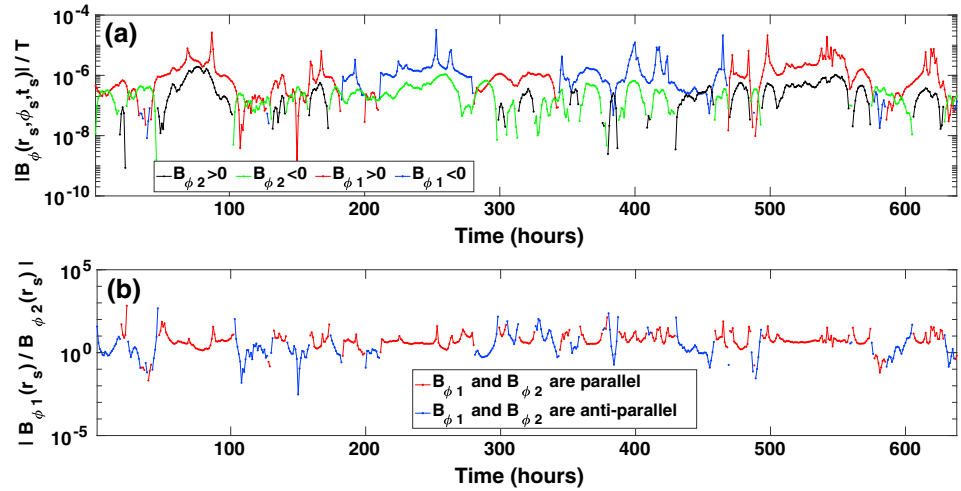
Figure 7. Variations of the predicted fields $|B_{\phi 1}(r_s, \phi_s, t_s)| = |B'_{\phi 1}(r'_s, \phi'_s)|$ and $|B_{\phi 2}(r_s, \phi_s, t_s)| = |B'_{\phi 2}(r'_s, \phi'_s)|$ with time (ϕ) for the period 1–27 August 2010, obtained with the new data-driven accelerating solar wind model and with the constant v_r solar wind model of Schulte in den Bäumen et al. (2011, 2012), respectively. (a) Red (blue) and black (green) dots show the magnitudes of $B_{\phi 1}(r_s, \phi_s, t_s)$ and $B_{\phi 2}(r_s, \phi_s, t_s)$ in the direction parallel (antiparallel) to the corotation direction, respectively. (b) Time variation of the ratio $|B_{\phi 1}(r_s, \phi_s, t_s)/B_{\phi 2}(r_s, \phi_s, t_s)|$ using red (blue) dots to show the components parallel (antiparallel) to the corotation direction. The average values of the ratios of the results from the two models are $\langle |B_{\phi 1}/B_{\phi 2}| \rangle \simeq 42.5$ and $\langle B_{\phi 1}/B_{\phi 2} \rangle \simeq -3.6$.

$\delta v_\phi(r_s, \phi_s, t_s) = 0$. The new accelerating solar wind model explains the predicted values of both the intrinsic $\delta v_\phi(r_s, \phi_s, t_s)$ and the intrinsic $B_\phi(r_s, \phi_s, t_s)$ in terms of the granulation and supergranulation cells predicting both the azimuthal flow and field components at the inner boundary.

Figure 8 compares the structural changes in $B_\phi(r_s, \phi_s, t_s)$ for the accelerating wind model with the results for the models of Schulte in den Bäumen et al. (2011, 2012), which assumed constant solar wind speed and did not conserve the angular momentum. The figure shows that the predictions differ not only in magnitude but also in direction. Accordingly, the differences in Figure 8 demonstrate that including angular momentum conservation, assuming an accelerating wind profile $v_\phi(r, \phi, t)$, and allowing a deviation $\delta v_\phi(r_s, \phi_s, t_s)$ from corotation, have important quantitative implications.
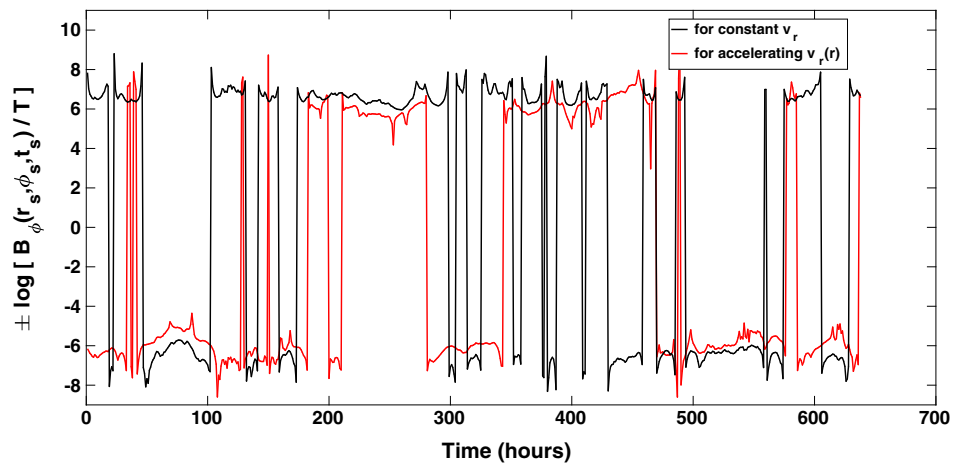
Figure 8. Extracted values of $B_\phi(r_s, \phi_s, t_s) = B'_\phi(r'_s, \phi'_s)$ for the constant (black) and accelerating (red) solar wind models for 1–27 August 2010 with 11 h boxcar smoothing, obtained by applying the data-driven solar wind models to Wind spacecraft data for $r_s = R_\odot$. We use the Schulte in den Bäumen et al. (2012) model for the constant solar wind. The vertical scale is $-\delta \log_{10} |B_\phi|$, with the field B_ϕ measured in tesla, and $\delta = +1$ for $B_\phi > 0$ and $\delta = -1$ for $B_\phi < 0$.
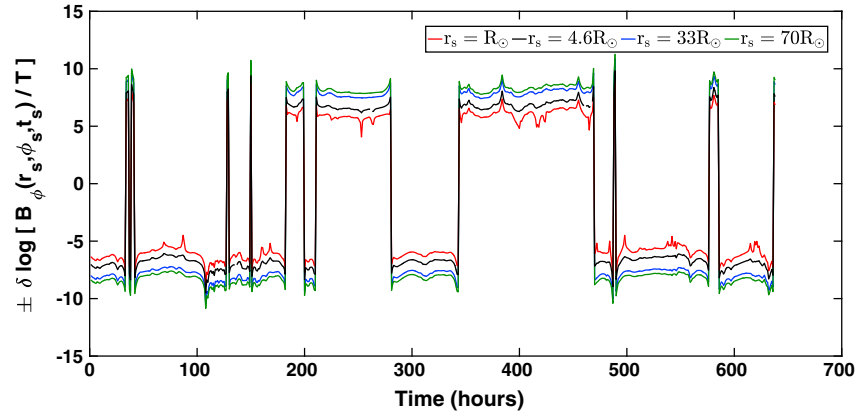
Figure 9. Extracted $B_\phi(r_s, \phi_s, t_s) = B_\phi(r_s', \phi_s')$ variations with time for different values of r_s obtained by applying the new data-driven accelerating solar wind model for the period 1–27 August 2010.

Figure 9 shows that changing the inner boundary distance r_s in the accelerating wind model does not cause structural changes in the predicted values of $|B_\phi(r_s, \phi_s, t_s)|$, only magnitude changes. Therefore, the model is robust with respect to reasonable choices of r_s. As expected from (67), the predicted magnitudes change with r_s since $B_\phi(r, \phi, t) \propto r^{-1}$. There is no consensus in the literature for the location of the inner boundary. Importantly, though, the new accelerating solar wind model is more flexible and viable for predicting the wind's properties than other models (e.g., Schulte in den Bäumen et al., 2011, 2012; Tasnim & Cairns, 2016) which constrain r_s to a certain distance. Note that Schulte in den Bäumen et al.'s (2011, 2012) models assumed $r_s > R_\odot$ whereas Tasnim & Cairns's (2016) model considered $r_s > r_A$.

5.3. Analytic Radial Variations of $B_\phi(r, \phi, t)$ and $v_\phi(r, \phi, t)$

The expressions (66) and (67) for $v_\phi(r, \phi, t)$ and $B_\phi(r, \phi, t)$ show that they are interrelated. In addition, $v_\phi(r, \phi, t)$ and $B_\phi(r, \phi, t)$ depend on $B_r(r, \phi, t)$ and on the intrinsic quantities $B_\phi(r_s, \phi_s, t_s)$, $B_r(r_s, \phi_s, t_s)$, and $v_\phi(r_s, \phi_s, t_s)$. Figure 10 shows the radial variations of $v_\phi(r, \phi_{ob}, t_{ob})$ and $B_\phi(r, \phi_{ob}, t_{ob})$ for various values of ϕ_{ob} during the period 1 to 27 August 2010, predicted using (66) and (67). Significant changes in both $v_\phi(r, \phi_{ob}, t_{ob})$ and $B_\phi(r, \phi_{ob}, t_{ob})$ occur for radii less than $r_A(\phi_{ob}, t_{ob})$, with ϕ_{ob} parameterized by time, while both $v_\phi(r, \phi_{ob}, t_{ob})$ and $B_\phi(r, \phi_{ob}, t_{ob})$ fall off as r^{-1} at large r ($r \gg r_A(\phi_{ob})$). Note that the gaps in the curves in Figures 9 and 10 correspond to the singularities at $r_A(\phi_{ob})$ expected from (66) and (67).
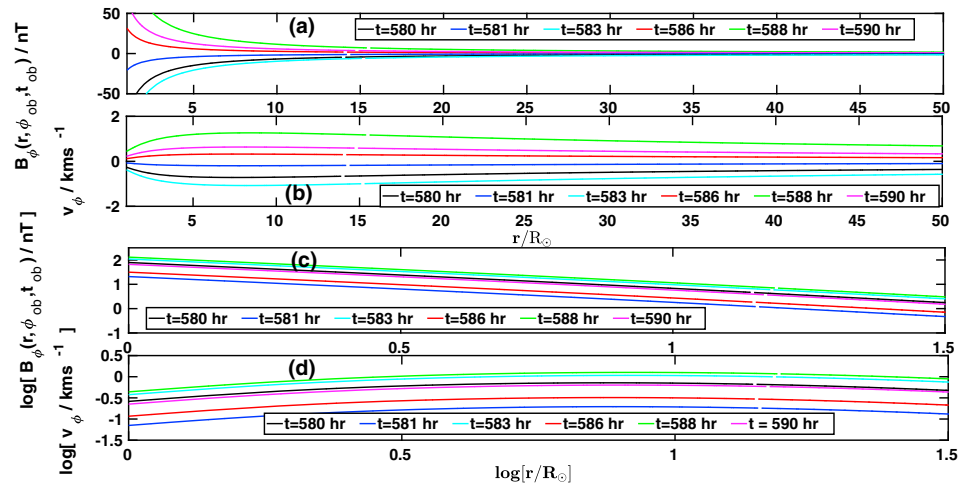
Figure 10. Radial variations of (a) $B_\phi(r, \phi, t)$ and (b) $v_\phi(r, \phi, t)$ using (67), (66), and 1 AU data for different phase angles $\phi(t)$ for the new accelerating solar wind model. Figure 10c shows the variations of log $|B_\phi(r, \phi, t)|$ with log$(r/R_\odot)$ and Figure 10d shows the variation of log $|v_\phi(r, \phi, t)|$ with log$[r/R_\odot]$, for the same phase angles.
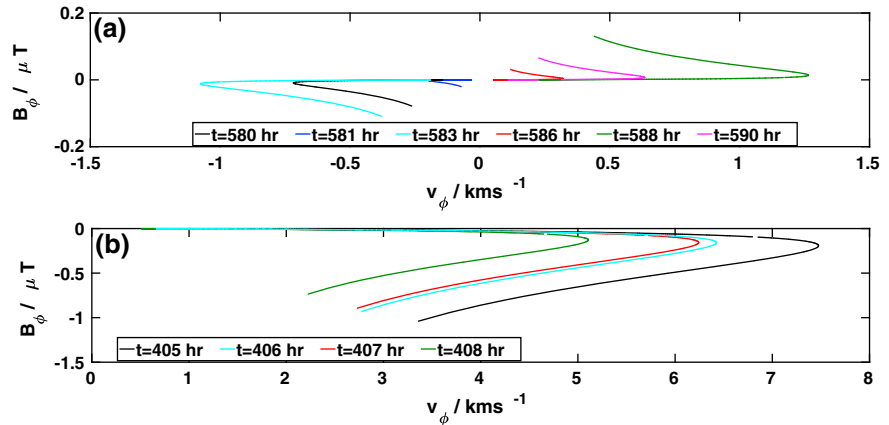
Figure 11. Variations of the predicted values of $B_\phi(r, \phi, t)$ with $v_\phi(r, \phi, t)$ for the new accelerating solar wind model for certain times during the period 1–27 August 2010. (a) Chosen phase angles $[\phi_{ob} = \phi_{ob}(t)]$ when $B_\phi(r, \phi, t)$ and $v_\phi(r, \phi, t)$ are in the same direction and (b) some chosen phase angles when $B_\phi(r, \phi, t)$ and $v_\phi(r, \phi, t)$ are oppositely directed.

Although $v_\phi(r, \phi_{ob}, t_{ob})$ and $B_\phi(r, \phi_{ob}, t_{ob})$ are coupled, (67) shows that $B_\phi(r, \phi_{ob}, t_{ob})$ can be oppositely directed to $v_\phi(r, \phi_{ob}, t_{ob})$ depending on the directions of $B_\phi(r_s, \phi_s, t_s)$, $\delta v_\phi(r_s, \phi_s, t_{ob})$ or $B_r(r_s, \phi_s, t_{ob})$. Figure 11a shows several values of $\phi_{ob} = \phi_{ob}(t)$ when v_ϕ and B_ϕ are in the same direction, whereas Figure 11b shows cases when v_ϕ and B_ϕ are oppositely directed to each other. As found by Weber and Davis (1967), $v_\phi(r, \phi)$ increases from $v_\phi(r_s, \phi_s, t_s)$ to a peak in the range $5\,R_\odot - 20\,R_\odot$ before decreasing at large r, always retaining the same sign at all r for a given ϕ_{ob}.

5.4. Angular Momentum per Unit Mass Variation With $t(\phi)$

Figure 12 shows that the time (ϕ) variations of the angular momentum per unit mass (L_z) predicted from (46) vary in the wide range of $10^{12}\,\mathrm{m}^2\,\mathrm{s}^{-1}$ to $10^{15}\,\mathrm{m}^2\,\mathrm{s}^{-1}$. The average magnitude of L_z is $\langle L_z \rangle \simeq 5 \times 10^{14}\,\mathrm{m}^2\,\mathrm{s}^{-1}$, which is larger than Weber and Davis's (1967) prediction of $L_{WD} = \Omega r_A^2 \simeq 1.5 \times 10^{14}\,\mathrm{m}^2\,\mathrm{s}^{-1}$. Note that Weber and Davis (1967) predicted $L_{WD} = \Omega r_A^2$ using $r_A = 10\,R_\odot$, whereas the new model predicts $\langle r_A \rangle \simeq 12\,R_\odot$. Importantly, using the expression $L_z = \Omega r_A^2$ with the new model's prediction for $r_A(\phi_a)$ yields values of L_z that are typically of very similar magnitudes to the new model's predictions, varying in the same range ($10^{12}\,\mathrm{m}^2\,\mathrm{s}^{-1}$ to $10^{15}\,\mathrm{m}^2\,\mathrm{s}^{-1}$) with the same average as the accelerating solar wind, but sometimes with structural changes in longitude. This implies that the magnitude of L_z mainly depends on $r_A(\phi_a)$ and that larger r_A provides the larger values of L_z, and vice versa. Notably, changes in sign of L_z are also evident in the new model, driven primarily by changes in the sign of $v_\phi(r_s, \phi_s, t_s)$ in (46).
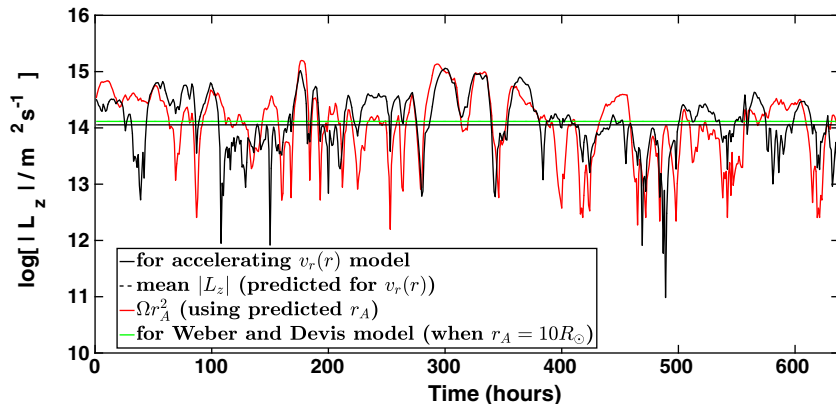
Figure 12. Predicted angular momentum per unit mass L_z carried away from the Sun for the period 1–27 August 2010 from the new accelerating solar wind model (black solid line). The black broken line shows the mean of L_z. Weber and Davis (1967) predicted $L_z = r_A^2 \Omega$ where $r_A = 10R_\odot$ (green line). The red line shows the value of $L_z = r_A^2 \Omega$ using the new model's prediction for $r_A(\phi_{ob})$, and the red broken line shows the corresponding mean.

An important quantitative result from Figure 12 is that L_z varies significantly in magnitude and direction with time/longitude. Physically, these significant variations should drive waves and turbulence in the solar wind, starting near the Sun but extending to 1 AU and beyond. Note that MHD waves and turbulent motions are known to be present from the low solar atmosphere out into the solar wind at 1 AU and beyond (Cranmer & van Ballegooijen, 2005; Tu & Marsch, 1995). In other words, the wind properties at the inner boundary predicted by the new accelerating wind model are highly variable and the large-scale variations in $L_z(\phi_{ob}, t_{ob})$ that are predicted should drive solar wind variability and turbulence from the Sun to 1 AU. This turbulence driver does not appear to be included in most turbulence models. Similarly, the predicted variability in L_z is not included in estimates of angular momentum loss from the Sun.

5.5. Electric Field in the Corotating Frame, E_z'

The new model allows intrinsic nonradial velocity, and magnetic field components at the inner boundary does not require a zero electric field E_z' in the corotating frame and also relaxes the assumption of corotation at the inner boundary. Noting that $\mathbf{B} = \mathbf{B}'$ in the nonrelativistic regime, the model yields $\mathbf{v}'$ and $\mathbf{B}'$ and so $\mathbf{E}'$ via (22). Fitting the model to the 1 AU data therefore allows us to test whether $\mathbf{E}_z' = 0$ and so $\mathbf{v}' \parallel \mathbf{B}'$ (where $\mathbf{B}' = \mathbf{B}$). Note that the standard theoretical assumption (e.g., Parker, 1958; Weber & Davis, 1967) is that $\mathbf{E}' = 0$.

Before fitting the new model to data, we revisit the alignment condition and the fields $\mathbf{E}'$ in the corotating frame in the models of Parker (1958), Weber and Davis (1967), Keppens and Goedbloed (1999), and Hu et al. (2003). We assume first that $E_\phi' \mathbf{e}_\phi + \mathbf{E}_p' \neq 0$, cf. (20). In the frozen-in approximation, the ϕ component yields

$$E_\phi' \mathbf{e}_\phi = \mathbf{v}_p' \times \mathbf{B}_p' = \mathbf{v}_p \times \mathbf{B}_p = 0. \tag{70}$$

Equation (70) demonstrates that the toroidal or azimuthal electric field vanishes in the corotating frame when $\mathbf{v}_p$ and $\mathbf{B}_p$ are aligned, and vice versa. Thus, the assumption of Keppens and Goedbloed (1999) and Hu et al. (2003) that the flow streamlines and magnetic field lines are aligned in the meridional plane requires $E'_\phi = 0$. Note that in the present model $v_\theta = B_\theta = 0$, so that $E_\phi' = 0$.

Rewriting (20), using (24) in the corotating frame

$$\mathbf{E}_p' = -\mathbf{v}_p \times B_\phi \mathbf{e}_\phi - (v_\phi - \Omega r)\mathbf{e}_\phi \times \mathbf{B}_p = 0. \tag{71}$$

Taking magnitudes and assuming $\mathbf{v}_p \cdot \mathbf{B}_p > 0$, (71) reduces to

$$B_\phi v_p = v_\phi B_p - \Omega r B_p = 0, \tag{72}$$

and we can then rearrange (72) in terms of the function Ω related to the electric field in Keppens and Goedbloed (1999)'s model, with

$$\Omega = \left(v_\phi - \frac{B_\phi v_p}{B_p} \right) / r. \tag{73}$$

Thus, (73) implies the assumption $\mathbf{E}_p' = 0$. Therefore, the combination of (71) and (73) together with $E_\phi = 0$ assumed by Keppens and Goedbloed (1999) are equivalent to the assumption $\mathbf{E}' = \mathbf{E}_p' + E_\phi' \mathbf{e}_\phi = 0$.

Now, we can also rewrite (71) as

$$\mathbf{E}_p' = E_r' \mathbf{e}_r + E_\theta' \mathbf{e}_\theta = (v_\phi - \Omega r)B_r \mathbf{e}_\theta - v_r B_\phi \mathbf{e}_\theta - (v_\phi - \Omega r)B_\theta \mathbf{e}_r + v_\theta B_\phi \mathbf{e}_r, \tag{74}$$

where $\mathbf{e}_r \times \mathbf{e}_\phi = -\mathbf{e}_\theta$, $\mathbf{e}_\phi \times \mathbf{e}_\theta = -\mathbf{e}_r$, and $\mathbf{e}_\theta \times \mathbf{e}_r = -\mathbf{e}_\phi$. The θ and r components of (71) and (74) can be written as

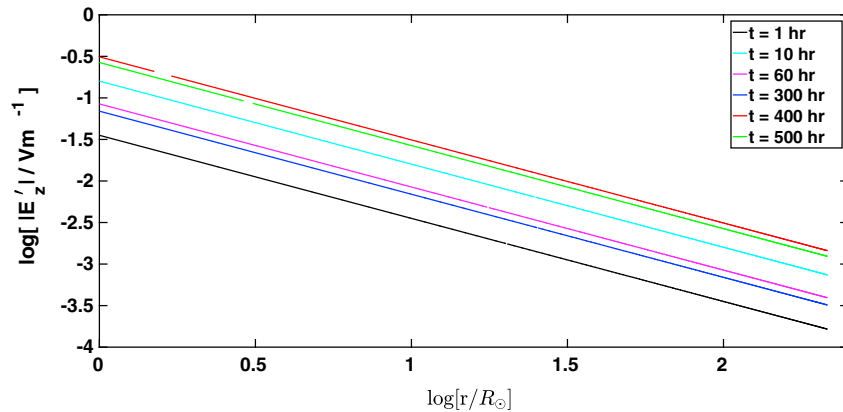$$E_\theta' = \left(-v_r B_\phi + (v_\phi - \Omega r \sin\theta)B_r \right), \tag{75}$$

and

$$E_r' = \left(v_r B_\phi - (v_\phi - \Omega r \sin\theta)B_r \right), \tag{76}$$

respectively.

The assumption $E_\theta' = 0$ allows us to rewrite (75) as

$$v_\phi - v_r B_\phi / B_r = \Omega r \sin\theta. \tag{77}$$

Figure 13. Radial variations of the electric field $E'_z \mathbf{z}$ in the corotating frame in the new accelerating solar wind model based on (22) and the Wind spacecraft's 1 AU data for six values of $t = t(\phi)$.

Equation (77) enforces the requirement that the θ component of the electric field in the corotating frame is zero. Hu et al. (2003) obtained (77) by analyzing the angular momentum conservation and implemented (77) in their analysis. Thus, Hu et al.'s (2003) analysis requires $E'_\theta = 0$. However, (76) suggests that a nonzero electric field component (E'_r) can still exist in the corotating frame in the Hu et al. (2003) model. In the model developed here, $E'_r = E'_\phi = 0$, but $E'_z \neq 0$.

Figure 13 shows the radial variation of E'_z predicted by (21) for several values of ϕ_{ob}, with E'_z along the $\pm z$ axes. Clearly, E'_z is high close to the Sun and decreases with increasing r as $|E'_z| \propto r^{-1}$. It is clear that $E'_z \neq 0$ at any r for this model; put another way, $\mathbf{v}'$ and $\mathbf{B}$ are not aligned in the corotating frame, contrary to the standard theoretical assumption (e.g., Jokipii & Kóta, 1998; Keppens & Goedbloed, 1999; Parker, 1958; Weber & Davis, 1967) or the assumption $E'_\theta = 0$ (this becomes the z axis component $E'_z = 0$ for our setup) of Hu et al. (2003).

The new model's predictions for E'_z at the inner boundary ($r_s = R_\odot$) are shown in Figure 14 for the period 1–27 August 2010. The figure shows that E'_z is often large at the inner boundary, with magnitudes that vary between 10^{-3} and 0.5 V. The consequences of high electric fields are explored in section 6.

5.6. Power Law Index, γ

In the model developed analytically in sections 3 and 4, an isothermal system is assumed so as to predict the accelerating wind profile $v_r(r, \phi, t)$. However, in reality the ion temperature close to the Sun is of the order of 1×10^6 K to 2×10^6 K, much higher than the range of temperatures' order of 2–20×10^4 K observed near 1 AU. We also assume a sonic point radius at $5\,R_\odot$, which is very close to the corona. Importantly,
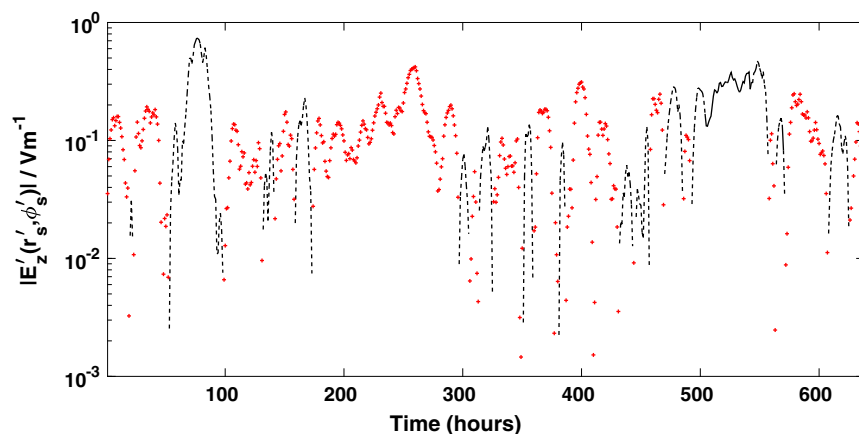
Figure 14. Time variation of $E'_z(r'_s, \phi'_s)$ for $r'_s = r_s = R_\odot$ in the corotating frame for the period 1–27 August 2010. Here the cross symbols show values of E'_z parallel to the z axis, while the dashed line shows values of E'_z antiparallel to the z axis.
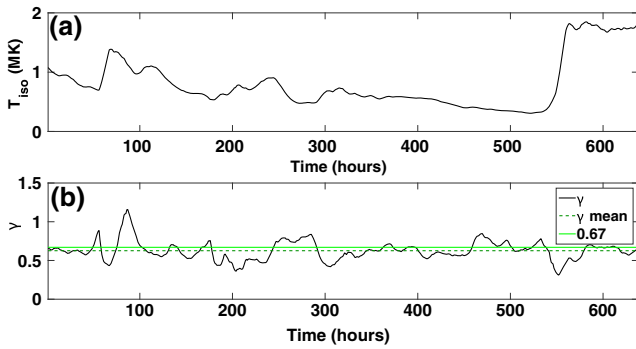
Figure 15. Time variations of the (a) sonic point temperature and (b) power law index γ predicted using (62) and (80), respectively, for the period 1–27 August 2010. In Figure 15b the dashed green line shows that the statistical mean of γ (0.64) is very close to the independent empirical value of 0.67 (Maksimovic et al., 1997b; Richardson & Paularena, 1997; Robinson & Cairns, 1998).

numerical solutions of (32) for power law temperature profiles $T_i(r)$ show relatively small changes in $v_r(r, \phi_{ob}, t_{ob})$ from the isothermal predictions (not shown).

Accordingly, for the purposes of better modeling the plasma, we now consider a power law model for $T_i(r)$ but retain the isothermal approximation for $v_r(r, \phi_{ob}, t_{ob})$. The power law model allows us to write the ion temperature as a function of r and ϕ:
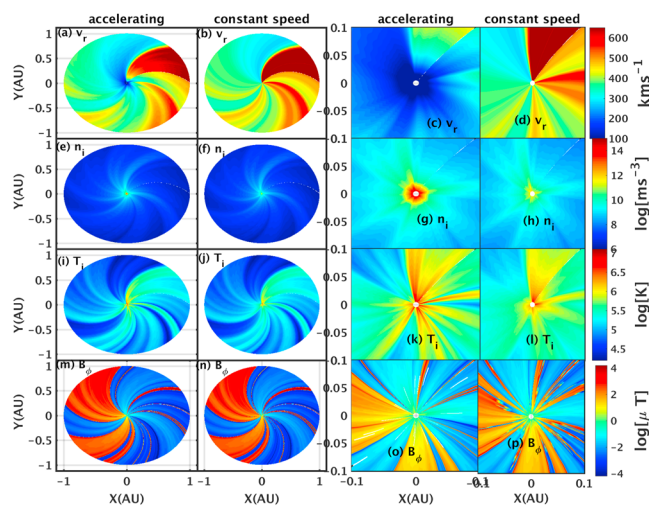
$$T_i(r, \phi, t) = T_i(r_{ob}, \phi_{ob}, t_{ob}) \left(\frac{r_{ob}}{r} \right)^{\gamma}. \qquad (78)$$

We can then find the power law index γ using the observed ion temperature at 1 AU, $T_i(r_{ob}, \phi_{ob}, t_{ob}) = T_{iob}$ and the prediction $T_i(r_{so}, \phi_{so}, t_{ob}) = T_{iso}$ at the sonic point r_{so} obtained from (63) using the observed values of $v_r(r_{ob}, \phi_{ob}, t_{ob})$, via

$$\frac{T_{iob}}{T_{iso}} = \left(\frac{r_{so}}{r_{ob}} \right)^{\gamma}, \qquad (79)$$

$$\gamma = \frac{\log \left(\frac{T_{iob}}{T_{iso}} \right)}{\log \left(\frac{r_{so}}{r_{ob}} \right)}. \qquad (80)$$

Figure 15 shows the variations with phase angle $\phi'_{ob} = \phi_{ob} - \Omega t_{ob}$ predicted for variations of the predicted (a) T_{iso} and (b) γ by fitting the model to the observed 1 AU data, using (62)–(80). The predicted values of T_{iso} are of the order of 0.5×10^6 K to 2×10^6 K, as expected for coronal temperatures. Moreover, the predicted values of γ vary between 0.25 and 1.25 with a statistical mean of 0.64. This mean is very close to the empirical power law index $\gamma \approx 0.67$ obtained in independent analyses of observational data (Maksimovic et al., 1997b; Richardson & Paularena, 1997; Robinson & Cairns, 1998).

5.7. Illustration of Global Plasma and Field Quantities

Predictions for solar wind quantities as functions of r and ϕ for both the accelerating and constant (Schulte in den Bäumen et al., 2012) solar wind models in the equatorial plane are shown in Figure 16 for the period 1 to 27 August 2010. Figures 16a, 16e, 16i, and 16m show how the extracted v_r, n_i, T_i, and B_{ϕ} vary with r and ϕ for the accelerating solar wind model from the Sun to 1 AU, while Figures 16c, 16g, 16k, and 16o zoom in the color plots for the preceding quantities to bring out the changes close to the Sun. Figures 16b, 16f, 16j, and 16n show the variations of v_r, n_i, $T_i(r)$, and B_{ϕ}, respectively, for Schulte in den Bäumen et al.'s (2011, 2012) model with a constant v_r, and Figures 16d, 16h, 16l, and 16p zoom in these quantities close to the Sun. Figure 16 shows clear evidence for the existence of corotating interaction region-like structures in the plasma quantities. For instance, in zones with high speeds ($\gtrsim 550$ km s^{-1}), densities ($\gtrsim 10^8$ m^{-3}), and temperatures ($\gtrsim 0.5 \times 10^6$ K) are clearly visible near $(X, Y) \simeq (1, 0)$, and $(X, Y) \simeq (0.8, 0.6)$. Comparing Figures 16c, 16g, 16k, and 16o, with Figures 16d, 16h, 16l, and 16p shows that the differences between the two models are significant near the inner boundary ($r_s = R_\odot$) where the solar wind is accelerating. Figures 16o and 16p show that the predictions for $B_{\phi}(r_s, \phi_s)$ from the two models not only have different magnitudes but also have slightly different magnetic sector changes (different sector structures are also clearly visible in Figure 8 when $r = r_s$).

Figure 17 displays the predicted (a) $v_{\phi}(r, \phi, t)$, (b) $\mathbf{L}(r, \phi, t)$, and (c) $E'_z(r', \phi')$ values for the new model, which allows a deviation from corotation. Figure 17a shows that $v_{\phi}(r, \phi, t)$ has notable variations with r and ϕ, and that the new model's predictions for $v_{\phi}(r, \phi, t)$ have significantly different structures than $B_{\phi}(r, \phi, t)$. These structural variations between the azimuthal flows and magnetic fields are manifestations of the existence of intrinsic, nonzero quantities
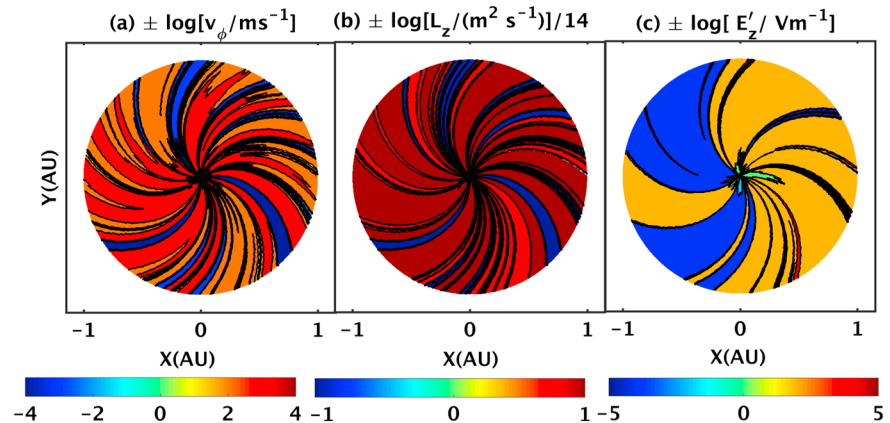

Figure 16. Predictions of the new model with an accelerating solar wind and comparison with the constant speed model of Schulte in den Bäumen et al. (2012). Shown are the (a, c) $v_r(r, \phi, t) = v'_r(r', \phi')$, (e, g) $n_i(r, \phi, t) = n'_i(r', \phi')$, (i, k) $T_i(r, \phi, t) = T_i(r', \phi')$, and (m, o) $B_{\phi}(r_s, \phi_s, t_s) = B'_{\phi}(r'_s, \phi'_s)$ for the accelerating solar wind model, whereas (b, d) $v_r(r, \phi, t)$, (f, h) $n_i(r, \phi, t)$, (j, l) $T_i(r, \phi, t) = T_i(r', \phi')$, and (n, p) $B_{\phi}(r, \phi, t) = B_{\phi}(r', \phi')$ are displayed for the constant speed solar wind using Schulte in den Bäumen et al.'s (2011, 2012) model. The two left-hand columns are for the domain $r = 1 R_\odot$ to 1 AU, whereas the two right-hand columns are for $|X| \le 0.1$ AU and $|Y| \le 0.1$ AU. The solar wind models are driven by Wind spacecraft data for the period 1–27 August 2010. The Sun is at $(X, Y) = (r \cos \phi, r \sin \phi) = (0, 0)$, and the Earth is at $r = 1$AU.

Figure 17. Predictions of the data-driven two-dimensional solar wind model for the period 1–27 August 2010: (a) $v_\phi(r, \phi, t)$, (b) $L_z(r, \phi, t)$, and (c) $E_z'(r', \phi')$, obtained using (66), (46), (22), respectively, and using the Wind spacecraft data. The Sun is at $(X, Y) = (r \cos \phi, r \sin \phi) = (0, 0)$, and the Earth is at $r = 1$AU. Note that positive values of $v_\phi(r, \phi, t)$ correspond to being directed in the corotation direction, and negative values correspond to $v_\phi(r, \phi, t)$ being oppositely directed. However, positive values of $L_z(r, \phi, t)$ and $E_z'(r', \phi')$ correspond to components directed upward along the z axis whereas the negative values represent downward components.

δv_ϕ and $B_\phi(r_s, \phi_s, t_s)$ at the inner boundary. Figure 17b shows that the predicted angular momentum is constant along a streamline but has strong variability with $\phi = \phi(t)$, which may provide a driver for solar wind turbulence, waves, and other disturbances from the inner boundary to 1 AU and beyond. Figure 17c shows the presence of $\mathbf{E}'(r', \phi') \neq 0$ at all r' and ϕ' in the corotating frame and that the predictions for E_z' vary strongly with r and $\phi = \phi(t)$. Note that the predicted E_z' field is along the $\pm z$ axes, that is, perpendicular to the solar equatorial plane.

6. Discussion and Conclusions

In the new model, the velocity $\mathbf{v}'$ in the corotating frame is allowed to have a component perpendicular to $\mathbf{B}'$, so that $\mathbf{E}' = \mathbf{v}' \times \mathbf{B}' \neq \mathbf{0}$ in general, but $\nabla \times \mathbf{E}' = 0$ is required (dashed variables are in the frame corotating with the Sun). However, the standard assumption (Weber & Davis, 1967) is that $\mathbf{v}'$ and $\mathbf{B}'$ are aligned, so that $E_z' = 0$. Similarly, as described in section 5, the solar wind model of Keppens and Goedbloed (1999) assumes $\mathbf{E}' = 0$ in the rotating frame, since the model assumes (73). However, the model of Hu et al. (2003) has a nonzero E_r' component in the rotating frame (as in equation (76)). It is appropriate to emphasize that the assumption $\mathbf{E}' = 0$ is stronger than the new model's assumption $\nabla \times \mathbf{E}' = \mathbf{0}$. A result of fitting the new model to data is that $E_z' \neq 0$ in general (Figures 13, 14, and 17), instead being significant at all r and ϕ. A consequence of finding $\mathbf{E}' \neq 0$ is that the field $\mathbf{E} = \mathbf{E}' - (\mathbf{v} - \mathbf{v}') \times \mathbf{B}$ and the quantity $\mathbf{E} \times \mathbf{B}$ in the inertial frame is changed compared with the case $\mathbf{E}' = 0$. Hence, the $\mathbf{E} \times \mathbf{B}$ particle drifts are changed, with consequences for particle energization and scattering. Note that the field $\mathbf{E}'$ in the new model is along z axis, that is, perpendicular to the equatorial plane, leading to standard charge-independent $\mathbf{E}' \times \mathbf{B}$ drifts in the equatorial plane.

Clearly, Figures 7–11 and 16 show strong r and ϕ variations of $\mathbf{B}$, so that nonzero gradients ∇B and curvatures of field lines exist. Thus, significant ∇B and curvature drifts are expected for particles with sufficient $v_\perp$ and $v_\parallel$, respectively. Crucially, these drifts are out of the plane and so either parallel or anti-parallel to $\mathbf{E}'$ in the present 2-D model. The drifting particles will then gain or lose energy due to the $\mathbf{E}'$ field (as they will for the standard assumed field $\mathbf{E} = -\mathbf{v}_{sw} \times \mathbf{B}$), with the gain/loss depending on the drift distance and the values of $v_\perp$ and $v_\parallel$ for the particles.

The changes in energy associated with these drifts can be large, depending on the directions of E_z' (and E_z), the drift distance (vector), $v_\perp$, and $v_\parallel$. For instance, with $|E_z'| \simeq 0.1$ V/m near r_s in Figure 14, if the ∇B or curvature drift moves the particle a distance d along $\mathbf{E}'$ then the energy charge $qE_z'd$ is of the order of 1 MeV for $d = 10^7 \simeq 0.01 R_\odot \simeq 10^{-5}$ AU. Such distances and energy changes appear plausible, with both smaller and larger values also possible. However, noting that E_z', $\mathbf{B}$, and ∇B vary significantly with ϕ and r (Figures 13, 14, and 17c), this effect may manifest itself mostly as heating and scattering processes due to particles having multiple episodes of energy gain and loss and having different drift velocities.

The new model assumes a constant spatial pattern of the solar wind for one solar rotation. If a spacecraft travels a distance $\Delta S_{1\,AU}$ in a time Δt along the Earth's orbit, forming an arc of angle $\Delta\theta$ at the center of the Sun, then $\Delta\theta = \Delta S_{\odot}/R_{\odot} = \Delta S_{1\,AU}/(1\,AU)$, where $\Delta S_{\odot}$ is the distance at the Sun's surface subtending the same angle. A spacecraft with an orbital speed equal to the Earth's ($V_{Earth} = 3 \times 10^4\,m\,s^{-1}$) moves a distance, $\Delta S_{1\,AU} = V_{Earth}\Delta t$ in a time Δt. Thus, we can write $\Delta S_{\odot} = V_{Earth}\Delta t R_{\odot}/1\,AU = 3 \times 10^4\,m\,s^{-1}\Delta t_{hr} \times 3600 \times 6.9 \times 10^8/1.5 \times 10^{11} \simeq 5 \times 10^5 \Delta t_{hr,1AU}\,m$ at the Sun. The average timescale of δv_{ϕ}'s sign changing is 10 h, which corresponds to a displacement of $\Delta S_{\odot} \approx 5 \times 10^6\,m \simeq 5\,Mm$. This displacement is comparable to the characteristic size of granules. The minimum timescale for the sign changing is 1 h, which results in a displacement of 0.5 Mm, and the maximum timescale is 40 h, which corresponds to a displacement of 20 Mm. These displacements for the maximum and minimum sign changing timescales are analogous to the cell sizes of supergranulation and granulation cells, respectively.

Granulation cells have a characteristic cell size of $S_{gran} \simeq 2\,Mm$ with a lifetime of the order of $T_{gran} \simeq 8 - 10\,min$, and supergranulation cells have a cell size of $S_{supergran} \simeq 30\,Mm$ with a lifetime of $T_{supergran} \simeq 24 - 48\,h$. The time and distance scales of granulation correspond to azimuthal speeds of the order of $v_{\phi\,gran} \simeq S_{gran}/T_{gran} \simeq 3\,kms^{-1}$ (Jokipii & Parker, 1968; Jokipii & Kóta, 1998), whereas supergranulation cells have azimuthal speed $v_{\phi\,supergran} \simeq S_{supergran}/T_{supergran} \simeq 0.2\,km\,s^{-1}$. The values of $v_{\phi}(r_s, \phi_s)$ predicted by fitting Wind spacecraft data to the accelerating solar wind model are thus comparable to the azimuthal velocities expected for granulation and supergranulation motions.

Note that the spacecraft is in an inertial frame in which the plasma quantities and the magnetic field components are time-dependent. Sections 2 and 3 relate variables in the inertial frame to the variables in the corotating frame in the text, and provide detailed transformations from one frame to the other. We also explain in section 2.2 that the time variations at 1 AU are only due to the rotation of a constant spatial pattern across the observer, which allows us to identify the time variations of $\delta v_{\phi}(r_s, \phi_s, t_s)$, with time and ϕ related by $\phi = \phi_s + \Omega(t - t_s)$. In addition, application of the model to spacecraft data leads to predict intrinsic azimuthal velocities that are comparable to the magnitudes of the nonradial/azimuthal velocities of granulation and supergranulation cells. Put in other words, the time and distance scales of convective cells and the predicted variations $\delta v_{\phi}(r_s, \phi_s, t_s)$ are not inconsistent, suggesting that convective photospheric cells are responsible for the azimuthal photospheric velocities obtained by applying the solar wind model to the Wind spacecraft data at 1 AU.

The effect of deviations from corotation at the inner boundary can be quantified using $\langle|\Delta v_{\phi\,dev}(1\,AU)|\rangle = \langle|v_{\phi}(1\,AU) - v_{\phi TC}(1\,AU)|\rangle$. This is the average of the differences in azimuthal velocity at 1 AU between the new model, which allows a deviation from corotation and includes an accelerating wind profile and a modified version of the Tasnim and Cairns (2016) model, which assumes corotation at the inner boundary (but now with an accelerating wind). For the period 1–27 August 2010, we have $\langle|\Delta v_{\phi\,dev}(1\,AU)|\rangle \simeq 1.6\,km\,s^{-1}$ with a standard deviation of 1.6 km s^{-1}. Another quantity to consider is the difference at 1 AU between the predicted $v_{\phi}(1AU)$ and the angular velocity $r_s^2\Omega/1\,AU$ predicted for $r = 1\,AU$ assuming corotation at the inner boundary and conservation of fluid angular momentum (Jokipii & Kóta, 1998; Schulte in den Bäumen et al., 2011, 2012). For this period $\langle|v_{\phi,L}(1\,AU)|\rangle = \langle|v_{\phi}(1\,AU) - r_s^2\Omega/1\,AU|\rangle \simeq 0.7\,km\,s^{-1}$ with a standard deviation of 0.5 km s^{-1}. The quantity $\langle|v_{\phi,L}(1\,AU)|\rangle$ ignores the peak of $v_{\phi}(r)$ at $r = r_A$, cf. Weber and Davis (1967) and Figures 10b and 10d. The results for $\langle\Delta v_{\phi,dev}(1\,AU)\rangle \neq 0$ and $\langle\Delta v_{\phi,L}(1\,AU)\rangle \neq 0$ support the interpretation that deviations from corotation are important, with observable consequences at 1 AU, although their statistical significance is relatively weak. The results are also inconsistent with the usual approximation of corotation at small r (e.g., Parker, 1958; Schulte in den Bäumen et al., 2011, 2012; Tasnim & Cairns, 2016; Weber & Davis, 1967).

The average absolute deviation of the observed azimuthal magnetic field at 1 AU from the Parker spiral is $\langle|\Delta B_{\phi\,dev}(1\,AU)|\rangle = \langle|B_{\phi}(1\,AU) + B_r(1\,AU)(1\,AU - r_s)\Omega/v_r(1\,AU)|\rangle \simeq 1.5\,nT \simeq \langle|B_r(1\,AU)|\rangle$ for the period 1–27 August 2010. This result shows that the azimuthal deviation from the Parker spiral is substantial at 1 AU and has the same magnitude as the radial magnetic field. Interestingly, the average absolute deviation of the observed $B_{\phi\,acc}(r, \phi, t)$ using (67) at 1 AU from the Parker spiral, $\langle|\Delta B_{\phi\,acc}(1\,AU)|\rangle \simeq \langle|B_{\phi\,acc}(r, \phi, t) + B_r(1\,AU)(1\,AU - r_s)\Omega/v_r(1\,AU)|\rangle \simeq 1.4\,nT \simeq \langle|\Delta B_{\phi\,div}(1\,AU)|\rangle$. Note that (67) shows that $\Delta B_{\phi}(1\,AU)$ at 1 AU is mainly due to the intrinsic velocities and that the magnetic fields at the inner boundary and magnitude of $\Delta B_{\phi}(1\,AU)$ at 1 AU also depend on the accelerating radial speed profile. Thus, it is not inconsistent to infer that the intrinsic nonradial magnetic fields and velocities at the inner boundary should lead to nonradial magnetic fields at 1 AU. A related inference is that $B_{\phi}(r_s, \phi_s, t_s)$ has significant effects on the azimuthal magnetic field

of the solar wind at any r. In other words, the new accelerating solar wind model relaxes the widely used assumptions of $\langle\Delta\delta v_\phi(r_s,\phi_s,t_s)\rangle \simeq 0$ (Parker, 1958; Schulte in den Bäumen et al., 2011, 2012; Tasnim & Cairns, 2016), and $\langle\Delta B_\phi(r_s,\phi_s,t_s)\rangle \simeq 0$ (Parker, 1958; Weber & Davis, 1967), and finds important effects due to the intrinsic azimuthal field and flow velocity.

The extracted $v_\phi(r_s,\phi_s,t_s)$ values vary significantly with r and ϕ (Figures 4–6, 10b, and 17). They demonstrate that a significant deviation from corotation is present. These deviations are close to zero when averaged over a solar rotation but have sufficient magnitude and sometimes cause the solar wind net azimuthal velocity to be directed opposite to the corotation direction. Put another way, the deviations from corotation significantly change the flow pattern and often prevent the solar wind from corotating.

Another result of this model is that L_z changes with $\phi(t)$. The substantial variability in L_z with ϕ, both in magnitude (a factor of 100) and direction suggest that the solar wind drives turbulence from near the Sun to 1 AU. Put another way, variabilities in photospheric and coronal sources of the solar wind should act as a source of vorticity and turbulence from the inner boundary outward.

In this new model, we assume plausible and general boundary conditions at the inner boundary, including acceleration of the solar wind, nonzero intrinsic azimuthal components of velocity and magnetic field, and a deviation from corotation. However, this remains a two-dimensional equatorial model, so it does not account for the latitudinal (θ) variation of the solar wind. The proposed SPP trajectory is nearly elliptical, only 3.4° from the ecliptic plane, and will approach to a perihelion distance of 8.5 $R_\odot$. Observations from SPP will thus be well suited to testing the model's predictions at the SPP's location, driven by 1 AU data. Similarly, observations from Solar Orbiter, Messenger, and BepiColombo can be used to test the model when near the equatorial plane.

Several three-dimensional global and numerical simulations (Cohen, 2015; Feng et al., 2015; Oran et al., 2013; Roussev et al., 2004; Schmidt et al., 2014; van der Holst et al., 2010) provide detailed models and predictions for the corona and the solar wind. However, these simulations assume purely radial solar wind at the inner boundary to initiate the simulations. One possible application of this paper's new data-driven accelerating solar wind model is to provide more realistic nonradial boundary values for the plasma velocity and magnetic field to initiate MHD simulations. Furthermore, the new model's predictions will enable us to test simulation results against theory, and vice versa.

In conclusion, a new accelerating solar wind model is presented that considers nonradial intrinsic velocities and magnetic fields from an inner boundary outward, relaxes the strong assumptions of corotation and zero electric field in the corotating frame, and imposes angular momentum conservation. Fitting the model to solar wind data for the period 1–27 August 2010 from the Wind spacecraft, we demonstrate that the new model predicts reasonable and consistent values of the Alfvénic critical radius (r_A), which are consistent with observations and shows global radial and longitudinal phase angle variations of the plasma and magnetic field quantities in the equatorial plane. The results depart significantly from the predictions of constant radial speed models (Schulte in den Bäumen et al., 2011, 2012; Tasnim & Cairns, 2016). This demonstrates that the accelerating profile for $v_r(r,\phi_{ob},t_{ob})$, and the nonzero intrinsic $\delta v_\phi(r_s,\phi_s,t_s)$ do have quantitative and qualitative effects on solar wind properties, especially close to the Sun. The new model predicts that the wind typically does not corotate at the inner boundary (or large radii), the electric field in the corotating frame has significant magnitudes at all r, and the field and angular momentum both vary, in sign and magnitude, with longitude.

Future work will compare the new model's predictions with MHD simulation results for the equatorial plane. Future improvements of the model will address the latitudinal variation of the wind, to provide a more complete three-dimensional picture of the solar wind, and to enable detailed comparison with 3-D simulation results.

Appendix A: Observations From the Wind Spacecraft

Figure A1 displays the observations of wind flow speed v_r, ion temperature T_i, ion number density n_i, **B**, and the r, θ, and ϕ components of **B** at 1 AU for the solar period of 1–27 August 2010 from the Wind spacecraft (Tasnim & Cairns, 2016). Note that the CME list "Near-Earth Interplanetary Coronal Mass Ejections since January 1996" compiled by Richardson and Cane (2015) shows a CME around hour 72.
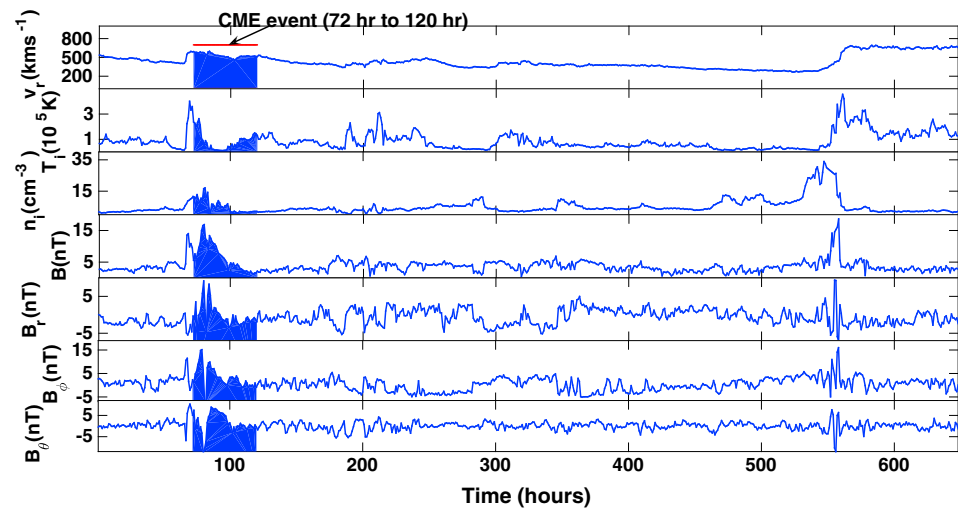
Figure A1. One hour averages of v_r(1 AU), T_i(1 AU), n_i(1 AU), B(1 AU), B_r(1 AU), B_ϕ(1 AU), and B_θ(1 AU), observed at 1 AU for the period 1–27 August 2010. The data are Wind spacecraft data accessed from CDAWeb with the magnetic components in HS (Heliocentric Solar) coordinates. The red bar above the top panel indicates the time when a CME is present.

References

Borovsky, J. E. (2010). On the variations of the solar wind magnetic field about the Parker spiral direction. *Journal of Geophysical Research*, *115*, A09101. https://doi.org/10.1029/2009JA015040

Bruno, R., & Carbone, V. (2005). The solar wind as a turbulence laboratory. *Living Reviews in Solar Physics*, *2*, 4.

Cohen, O. (2015). Quantifying the difference between the flux-tube expansion factor at the source surface and at the Alfvén surface using a global model for the solar wind. *Solar Physics*, *226*, 2245–2263.

Cohen, O., Sokolov, I. V., Roussev, I. I., & Gombosi, T. I. (2007). A semi-empirical magnetohydrodynamic model of the solar wind. *Astrophysical Journal*, *645*, L163—L166.

Cohen, O., Sokolov, I. V., Roussev, I. I., & Gombosi, T. I. (2008). Validation of a synoptic solar wind model. *Journal of Geophysical Research*, *113*, A03104. https://doi.org/10.1029/2007JA012797

Coles, W. A. (1995). Interplanetary scintillation observations of the high-latitude solar wind. *Space Science Reviews*, *72*, 211–222.

Cranmer, S. R. (2002a). Coronal holes and the high-speed solar wind. *Space Science Reviews*, *101*, 229–294.

Cranmer, S. R. (2002b). Solar wind acceleration in coronal holes. In *Proceedings of the SOHO-11 Symposium: From solar minimum to solar maximum* (pp. 361–366). Noordwijk: ESA SP-508.

Cranmer, S. R., & van Ballegooijen, A. A. (2005). On the generation, propagation, and reflection of Alfvén waves from the solar photosphere to the distant heliosphere. *Astrophysical Journal Supplement*, *156*, 265–293.

DeForest, C. E., Howard, T. A., & McComas, D. J. (2014). Inbound waves in the solar corona: A direct indicator of Alfvén surface location. *Astrophysical Journal*, *787*, 124.

De Pontieu, B., McIntosh, S. W., Carlsson, M., Hansteen, V. H., Tarbell, T. D., Boerner, P., ... Title, A. M. (2011). The origins of hot plasma in the solar corona. *Science*, *331*, 55–58.

Downs, C., Roussev, I. I., Van Der Holst, B., Lugaz, N., Sokolov, I. V., & Gombosi, T. I. (2010). Toward a realistic thermodynamic magnetohydrodynamic model of the global solar corona. *Astrophysical Journal*, *712*, 1219–1231.

Farrell, W. M., Thompson, R. F., Lepping, R. P., & Byrnes, J. B. (1995). A method of calibrating magnetometers on a spinning spacecraft. *IEEE Transactions on Magnetics*, *31*(2), 966–972.

Feng, X., Ma, X., & Xiang, C. (2015). Data-driven modeling of the solar wind from 1 r_s to 1 AU. *Journal of Geophysical Research: Space Physics*, *120*, 159–174. https://doi.org/10.1002/2015JA021911

Fisk, L. A. (1996). Motion of the footpoint of the heliospheric magnetic field lines at the Sun: Implications for recurent energetic particle events at high heliographic latitude. *Journal of Geophysical Research*, *101*, 15,547–15,553.

Forsyth, R. J., Balogh, A., Horbury, T. S., Erdos, G., Smith, E. J., & Burton, M. E. (1996). The heliospheric magnetic field at solar minimum: Ulysses observations from pole to pole. *Astronomy and Astrophysics*, *316*, 287–295.

Goldstein, M. L., & Roberts, D. A. (1995). Magnetohydrodynamic turbulence in the solar wind. *Annual Review of Astronomy and Astrophysics*, *33*, 283–325.

Groth, C. P. T., DeZeeuw, D. L., Gombosi, T. I., & Powell, K. G. (2000). Global three-dimensional MHD simulation of a space weather event: CME formation, interplanetary coronal mass ejections at one AU during 1995–2004. *Journal of Geophysical Research*, *105*, 25,053–25,078.

Hakamada, K., & Kojima, M. (1994). Solar wind speed and its acceleration inferred using the interplanetary scintillation method in Carrington rotation 1753. *Solar Physics*, *153*, 419.

Jokipii, J. R., & Kóta, J. (1998). The polar heliospheric magnetic field. *Geophysical Research Letters*, *16*, 1–4.

Jokipii, J. R., & Parker, E. N. (1968). Random walk of magnetic lines of force in astrophysics. *Physical Review Letters*, *21*, 44–47.

Keppens, R., & Goedbloed, J. P. (1999). Numerical simulations of stellar winds. *Space Science Reviews*, *87*, 223–226.

Kohl, J. L., Noci, G., Antonucci, E., Tondello, G., Huber, M. C. E., Gardner, L. D., ... Smith, P. L. (1997). First results from the SOHO Ultraviolet Coronagraph Spectrometer. *Solar Physics*, *175*, 613–644.

Leinweber, H. K., Russell, C. T., Torkar, K., Zhang, T. L., & Angelopoulos, V. (2008). An advanced approach to finding magnetometer zero levels in the interplanetary magnetic field. *Measurement Science and Technology*, *19*, 055104.

Lepping, R. P., Acuna, M. H., Burlaga, L. F., Farrell, W. M., Slavin, J. A., Schatten, K. H., ... Worley, E. M. (1995). The wind magnetic field investigation. *Space Science Reviews*, *71*, 207–229.

Li, B., Cairns, I. H., Gosling, J. T., Malaspina, D., Neudegg, D., Steward, G., & Lobzin, V. (2016). Comparisons of mapped magnetic field lines with the source path of the 7 April 1995 type III solar radio burst. *Journal of Geophysical Research: Space Physics*, *121*, 6141–6156. https://doi.org/10.1002/2016JA022756

Li, B., Cairns, I. H., Gosling, J. T., Steward, G., Francis, M., Neudegg, D., ... Milne, A. (2016). Mapping magnetic field lines between the Sun and Earth. *Journal of Geophysical Research: Space Physics*, *121*, 925–948. https://doi.org/10.1002/2015JA021853

Linker, J. A., Riley, P., Mikiċ, Z., Biesecker, D. A., Gibson, S. E., Forsyth, R. J., ... Thompson, B. J. (1999). Magnetohydrodynamic modeling of the solar corona during whole Sun month. *Journal of Geophysical Research*, *104*, 9809–9830.

Maksimovic, M., Pierrard, V., & Lemaire, J. F. (1997b). A kinetic model of the solar wind with Kappa distribution functions in the corona. *Astronomy and Astrophysics*, *324*, 725–734.

Mikiċ, Z., Linker, J. A., Schnack, D. D., Lionello, R., & Tarditi, A. (1999). Magnetohydrodynamic modeling of the global solar. *Physics of Plasmas*, *6*, 2217–2224.

Neugebauer, M., Liewer, P. C., Smith, E. J., Skoug, R. M., & Zurbuchen, T. H. (2002). Sources of the solar wind at solar activity maximum. *Journal of Geophysical Research*, *107*(A12), 1488. https://doi.org/10.1029/2001JA000306

Oran, R., van der Holst, B., Landi, E., Jin, M., Sokolov, I. V., & Gombosi, T. I. (2013). A global wave-driven magnetohydrodynamic solar model with a unified treatment of open and closed magnetic field topologies. *Astrophysical Journal*, *778*, 176.

Parker, E. N. (1958). Dynamics of the interplanetary gas and magnetic fields. *Journal of Astrophysics*, *128*, 664–676.

Petrie, G. J. D., & Patrikeeva, I. (2010). A comparative study of magnetic field in the solar photosphere and chromosphere at equatorial and polar latitudes. *Astrophysical Journal*, *699*, 781.

Hu, Q. Y., Li, X., & Habbal, S. R. (2003). A 2.5-dimensional MHD Alfvėn-wave-driven solar wind model. *Journal of Geophysical Research*, *108*(A10), 1378. https://doi.org/10.1029/2003JA009889

Richardson, J. D., Belcher, J. W., Lazarus, A. J., Paularena, K. I., Steinberg, J. T., & Gazis, P. R. (1996). Non-radial flows in the solar wind, *Proceedings of eight solar wind* (Vol. 382, pp. 479). Woodbury, NY: American Institute of Physics.

Richardson, I., & Cane, G. H. V. (2015). Near-earth interplanetary coronal mass ejections since January 1996. Retrieved from http://www.srl.caltech.edu/ACE/ASC/DATA/level3/icmetable2.htm, Updated September 22, 2015

Richardson, J. D., & Paularena, K. I. (1997). Streamer belt structure at solar minima. *Geophysical Research Letters*, *24*, 1435–1438.

Robinson, P. A., & Cairns, I. H. (1998). Fundamental and harmonic emission in type III solar radio bursts III. heliocentric variation of interplanetary beam and source parameters. *Solar Physics*, *181*, 363.

Roussev, I. I., Gombosi, T. I., Sokolov, I. V., Velli, M., Manchester, W., DeZeeuw, D. L., ... Luhmann, J. (2003). Decline and recovery of the interplanetary magnetic field during the protracted solar minimum. *Astrophysical Journal*, *595*, L57—L61.

Roussev, I. I., Sokolov, I. V., Forbes, T. G., Gombosi, T. I., Lee, M. A., & Sakai, J. I. (2004). A numerical model of a coronal mass ejection: Shock development with implications for the acceleration of GeV protons. *Astrophysical Journal*, *605*, L73—L76.

Schmidt, J. M., Cairns, I. H., & Lobzin, V. V. (2014). The solar type II radio bursts of 7 March 2012: Detailed simulation analyses. *Journal of Geophysical Research: Space Physics*, *119*, 6042–6061. https://doi.org/10.1002/2014JA019950

Schulte in den Bäumen, H., Cairns, I. H., & Robinson, P. A. (2011). Modeling 1 AU solar wind observations to estimate azimuthal magnetic fields at the solar source surface. *Geophysical Research Letters*, *38*, L24101. https://doi.org/10.1029/2011GL049578

Schulte in den Bäumen, H., Cairns, I. H., & Robinson, P. A. (2012). Nonzero azimuthal magnetic fields at the solar source surface: Extraction, model, and implications. *Journal of Geophysical Research*, *117*, A10104. https://doi.org/10.1029/2012JA017705

Smith, E. J. (1979). Interplanetary magnetic fields. *Reviews of Geophysics*, *17*, 610–623.

Suess, S. T., Wang, A. H., Wu, S. T., Poletto, G., & McComas, D. J. (1999). A two-fluid MHD coronal mode. *Journal of Geophysical Research*, *104*, 4697–4708.

Tasnim, S., & Cairns, I. H. (2016). An equatorial solar wind model with angular momentum conservation and non-radial magnetic fields and flow velocities at an inner boundary. *Journal of Geophysical Research: Space Physics*, *121*, 4966–4984. https://doi.org/10.1002/2016JA022725

Thomas, B. T., & Smith, E. J. (1980). The Parker spiral configuration of the interplanetary magnetic field between 1 and 8.5 AU. *Journal of Geophysical Research*, *85*, 6861–6867. https://doi.org/10.1029/JA085iA12p06861

Tu, C.-Y., Zhou, C., Marsch, E., Xia, L.-D., Zhao, L., Wang, J.-X., & Wilhelm, K. (2005). Solar wind origin in coronal funnels. *Science*, *308*, 519–523.

Tu, C. Y., & Marsch, E. (1995). MHD structures, waves and turbulence in the solar wind: Observations and theories. *Solar Physics*, *171*, 363–391.

Usmanov, A. V. (1993). A global numerical 3-D MHD model of the solar wind. *Solar Physics*, *146*, 377–396.

Usmanov, A. V., & Goldstein, M. L. (2003). A tilted-dipole MHD model of the solar corona and solar wind. *Journal of Geophysical Research*, *108*(A9), 1354. https://doi.org/10.1029/2002JA009777

Usmanov, A. V., Goldstein, M. L., Besser, B. P., & Fritzer, J. M. (2000). A global MHD solar wind model with WKB Alfvėn waves: Comparison with Ulysses data. *Journal of Geophysical Research*, *105*, 12,675–12,696.

van der Holst, B., Manchester IV, W. B., Frazin, R. A., Vásquez, A. M., Tóth, G., & Gombosi, T. I. (2010). A data-driven, two-temperature solar wind model with Alfvėn waves. *Astrophysical Journal*, *725*, 1373–1383.

Weber, E. J., & Davis, L. (1967). The angular momentum of the solar wind. *Astrophysical Journal*, *148*, 217.

Wu, S. T., Guo, W. P., Michels, D. J., & Burlaga, L. F. (1999). MHD description of the dynamic relationships between a flux rope, streamer corona mass ejection, and magnetic cloud: An analysis of the January 1997 Sun-Earth connection event. *Journal of Geophysical Research*, *104*, 14,786–14,802.

Zank, G. P., & Matthaeus, W. H. (1991). Nearly incompressible fluids. I. Hydrodynamics, turbulence and waves. *Physics of Fluids A*, *3*, 69–82.

Zank, G. P., & Matthaeus, W. H. (1992). Waves and turbulence in the solar wind. *Journal of Geophysical Research*, *97*, 17,189–17,194.

Zank, G. P., & Matthaeus, W. H. (1993). Nearly incompressible fluids. III: Magnetohydrodynamics, turbulence and waves. *Physics of Fluids A*, *5*, 257–273.